Quantifying the impacts of ENSO and IOD on rain gauge and remotely sensed precipitation products over Australia

E. Forootan[a,b], Khandu[b], J.L. Awange[b,c,f], M. Schumacher[a], R. Anyah[d], A.I.J.M. van Dijk[e], J. Kusche[a]

[a] *Institute of Geodesy and Geoinformation, University of Bonn, Bonn, Germany*
[b] *Department of Spatial Sciences, University of Curtin, Perth, Australia*
[c] *Karlsruhe Institute of Technology, Karlsruhe, Germany*
[d] *Department of Natural Resources and the Environment, University of Connecticut, USA*
[e] *Fenner School of Environment and Society, The Australian National University, Canberra, Australia*
[f] *Department of Geophysics, Kyoto University, Kyoto Japan*

Abstract

Large-scale ocean-atmospheric phenomena like the El Niño Southern Oscillation (ENSO) and Indian Ocean Dipole (IOD) have significant influence on Australia's precipitation variability. In this study, multi-linear regression (MLR) and complex empirical orthogonal function (CEOF) analyses were applied to isolate (i) the continental precipitation variations likely associated with ENSO and IOD, here referred to as 'ENSO/IOD mode', and (ii) the variability not associated with ENSO/IOD (the 'non-ENSO/IOD mode'). The first is of interest due to its dominant influence on inter-annual variability, while the second may reveal lower frequency variability or trends. Precipitation products used for this study included gridded rainfall estimates derived by interpolation of rain gauge data from the Australian Bureau of Meteorology (BoM), two satellite remote sensing products (CHIRP and TRMM TMPA version 7), and two weather forecast model re-analysis products (ERA-Interim and MERRA). The products covered the period 1981-2014 except TMPA (1998-2014). Statistical and frequency-based inter-comparisons were performed to evaluate the seasonal and long-term skills of various rainfall products against the BoM product. The results indicate that linear trends in rainfall during 1981-2014 were largely attributable to ENSO and IOD. Both intra-annual and seasonal rainfall changes associated with ENSO and IOD increased from 1991 to 2014. Among the continent's 13 major river basins, the greatest precipitation variations associated to ENSO/IOD were found over the Northern and North East Coast, while the smallest contributions were for Tasmania and the South West Coast basins. We also found that although the assessed products show comparable spatial variability of rainfall over Australia, systematic seasonal differences exist that were more pronounced during the ENSO and IOD events.

Keywords: Australia's Rainfall, Remote Sensing, long-term trend, Complex EOF, ENSO, IOD, Seasonal bias

1. Introduction

Rainfall variability significantly influences water resource availability over the Australian continent. It also has caused drought and flood events over the past decades, including a prolonged multi-year drought from 1995 to 2009 known as the 'Millennium drought' (Ummenhofer et al., 2009a; van Dijk et al., 2013); a shift to drier conditions in southwest Western Australia since the 1970s (Raut et al., 2014), and a period of widespread flooding over the eastern regions from 2009 to 2012 (Boening et al., 2012).

Australia is surrounded by tropical and subtropical oceans, and its climate is sensitive to large-scale ocean-atmosphere interactions. El Niño Southern Oscillation (ENSO) and Indian Ocean dipole (IOD) phenomena have been known to significantly influence precipitation over Australia (Trenberth, 1990; Nicholls et al., 1997), and also influence other regions of the world, e.g., Africa (Awange et al., 2013;

Email address: forootan@geod.uni-bonn.de (E. Forootan)

Omondi et al., 2013; Bloszies and Forman, 2015) and South America (de Linage et al., 2013; Córdoba-Machado et al., 2015). ENSO is mainly generated through movements of the tropical convergence zones from their seasonal mean positions, causing tropical and extra tropical responses (Cai et al., 2012). Although sea surface temperature (SST) in the tropical Indian Ocean co-varies with that of the tropical Pacific, IOD itself is known as a distinguishable phenomenon that can act to enhance or mitigate ENSO and contributes to inter-annual variability of rainfall over Australia (Saji et al., 1999). ENSO conditions often develop in austral winter and spring and tends not to peak until austral summer. In contrast, IOD develops in winter and typically becomes stronger during austral spring when it is correlated with ENSO (Ummenhofer et al., 2009a; Cai et al., 2012). Hence, the independent and combined impacts of ENSO and IOD exist in all seasons, which makes it difficult to separate their contribution to rainfall changes and consequently water storage variability over the Australian continent.

The impact of ENSO on Australian rainfall has been known for decades (e.g., Walker, 1923; Nicholls, 1985). The influence of IOD on Australian climate has also been reported in previous studies such as Ashok et al. (2003a) and Ummenhofer et al. (2009a,b). Most of these studies, however, have focused on describing the underlying mechanisms for the transmission of ENSO and IOD to Australian climate (e.g., Cai et al., 2011), rather than quantifying spatial and temporal rainfall changes due to (or in the absence of) these phenomena.

Here, we hypothesize that the annual and semi-annual rainfall variability computed from long-term (∼30 years) precipitation data represents the mean seasonality of climate variability over the Australian continent. The impact of ENSO and IOD can be considered an additional superimposed variability that changes the amplitude and potentially the phase of 'non-(normal) seasonal' precipitation variability over the continent. This assumption is in line with previous studies that quantified rainfall variability or water resources such as Chiew et al. (1998) and Power et al. (1999), who estimated rainfall variability due to the inter-decadal variability of ENSO and its modulations.

Long-term rainfall trends over Australia were discussed in Smith (2004), Smith et al. (2009), van Dijk et al. (2013), and Fu et al. (2010). Furthermore, Liu et al. (2007, 2009) and Bauer-Marschallinger et al. (2013) quantified the influence of ENSO and IOD on remotely sensed surface soil moisture and vegetation water content variations, while Garćia-Garćia et al. (2011) and Forootan et al. (2012) studied water storage variations since 2003 estimated from Gravity Recovery and Climate Experiment (GRACE) observations to define the regions that are predominantly affected by ENSO and IOD.

This study adds to previous efforts by studying three decades (1981-2014) of monthly gridded precipitation products to assess seasonal, inter- and intra-annual variability of precipitation over Australia. The relationships between these changes and ENSO/IOD events are addressed. The products include: gridded monthly precipitation estimates derived by interpolation of rain gauge measurements produced by the Australian Bureau of Meteorology (BoM, Jones et al., 2009), a recent satellite remote sensing product of the Climate Hazards Group Precipitation (CHIRP, Funk et al., 2014), monthly products of the Tropical Rainfall Measuring Mission (TRMM Multi-satellite Precipitation Analysis (TMPA) version 7, Huffman et al., 2007) that incorporate guage measurements, as well as the weather forecast model re-analysis products ERA-Interim from the European Centre for Medium-Range Weather Forecasts (Dee et al., 2011), and the Modern-Era Retrospective Analysis for Research and Applications (MERRA) from NASA (Rienecker et al., 2011).

The mentioned products were selected because they are long-term gridded products that have been used in several previous continental-wide rainfall estimation studies (e.g., Fleming and Awange, 2013; Renzullo et al., 2011; Peña-Arancibia et al., 2013; Pipunic et al., 2013), climate studies (e.g., Ashcroft et al., 2013; Donat et al., 2014), water storage monitoring studies (Rieser et al., 2011; Awange et al., 2011; Forootan et al., 2012; Seoane et al., 2013), or as input of hydrological models (e.g., Gebremichael and Zeweldi, 2007; Peña-Arancibia et al., 2011; van Dijk and Renzullo, 2011; van Dijk et al., 2011). CHIRP is a long-term satellite-only rainfall product that has been applied here for the first time over Australia. Estimation of rainfall over Australia, similar to other parts of the world, is vulnerable to errors during both anomalously dry (Dai, 2013) and wet conditions (e.g., Bosilovich et al., 2008; Trenberth, 2011, cf. *http : //www.cawcr.gov.au/projects/SatRainVal/sat_val_aus.html*). Pipunic et al. (2013) reported that estimates of rainfall from different satellite observations can be very different, particularly over tropical areas with high precipitation. Therefore, an incorporation of gauge observations to correct the biases of satellite rainfall (e.g., Ebert et al., 2007; Peña-Arancibia et al., 2011), or a complementary use

of gauge, reanalysis, and satellite rainfall products is desired (Peña-Arancibia et al., 2013).

In order to understand the seasonal to long-term behavior of rainfall variability over Australia, three main objectives are drawn here that include: (i) quantifying the variability of rainfall due to ENSO and IOD events (here called the 'ENSO/IOD mode' of rainfall) to address the amount of precipitation over the continent due to these major phenomena, (ii) removing the impacts of ENSO and IOD from rainfall variability ('non-ENSO/IOD mode' of rainfall) and analyzing the underlying large-scale rainfall variability, trend and seasonality, and (iii) quantifying the ability of satellite and reanalysis products to accurately represent seasonal precipitation as well as the major climatic phenomena of ENSO and IOD. Objective (ii) has not often been addressed in previous studies while (i) has been of particular interest due to its dominant impact. In addition to fully spatial analysis, we also report our results for Australia's major river basins (Figure 1).

To estimate the impact of ENSO and IOD on spatio-temporal rainfall variability, two independent techniques were considered. First, a multi-linear regression (MLR) technique was applied with the main assumption that the temporal patterns of ENSO and IOD, respectively derived from Niño 3.4 (`http://www.cpc.ncep.noaa.gov/products/analysis_monitoring/ensostuff/`) and Dipole Mode Index (DMI, `http://www.jamstec.go.jp/e/`), directly influence monthly accumulated rainfall changes. Since it is expected that different phases of ENSO and IOD might also have impacts on rainfall changes, Hilbert transformation of the ENSO and IOD indices was used to account for the phase lag (see Section 4.1). The indices and their Hilbert-transformed patterns along with a linear trend, annual, and semi-annual cycles were fitted to the time series of gridded precipitation products using MLR (see also Phillips et al., 2012). Thereby, amplitudes and phase propagations of ENSO/IOD mode were estimated. The non-ENSO/IOD mode was calculated as residuals of the total rainfall variations and the ENSO/IOD mode. The impact of ENSO and IOD was alternatively extracted from rainfall time series by applying the statistical method of complex empirical orthogonal function (CEOF, Rasmusson et al., 1981). Unlike the MLR technique, the CEOF technique does not require a priori assumptions about the variability of ENSO/IOD mode, and has been successfully used to explore SST (e.g., Enfield and Mestas-Nuñez, 1999) and water storage variations (e.g., Bauer-Marschallinger et al., 2013; Forootan, 2014). By applying CEOF, one can extract both temporal and spatial propagation of precipitation patterns that are associated to ENSO/IOD, while by applying MLR only the temporal phase propagation of precipitation changes (due to ENSO/IOD) is considered.

In order to address our objective (iii), we used the gridded BoM estimates as our reference 'truth'. The spatial representation (in terms of spatial correlations) of various satellite rainfall products were compared to BoM estimates. The skill of the satellite products in representing seasonal and non-seasonal precipitation changes were also assessed against BoM products.

The remaining part of this study is organized as follows: in Section 2 the Australian climate is explained. In Section 3, the datasets of the study are introduced, and the methodology of their analysis is explained in Section 4. The results are reported in Section 5, and finally, the study is summarized and concluded in Section 6.

2. Australian climate

The Australian continent experiences a variety of climatic conditions ranging from wet tropical conditions in the north, arid conditions in the interior, to temperate sub-humid to humid conditions in the south. Six climate zones (see, Figure 1a) were identified by Stern et al. (2000) based on a modified Köppen classification system applied to 30-year (1961-1990) mean rainfall, maximum and minimum temperature, and elevation.

The amount of precipitation in Australia is less than other inhabited continents on Earth. Climate is strongly influenced by the surrounding open oceans, including the southwestern Pacific Ocean in the east and the Indian Ocean in the west. Tropical cyclones are a prominent feature in the coastal regions of the northern and north-eastern Australia, while the western and central regions remain relatively dry (e.g., Sturman and Tapper, 1996). The Great Dividing Range along the coast of southeast Australia is the main topographic feature (elevation <2208 m above sea level) but has modest influence on large-scale weather systems other than creating local orographic rainfall gradients.

The impacts of ENSO and IOD on the climate of Australia have been found dominant on inter- and

intra-annual variability of rainfall in various regions. During El Niño (negative phase on ENSO), northern and eastern parts of Australia experience reduced rainfall and often prolonged drought in the interior regions (e.g., during 1997-1998). Conversely, La Niña periods often result in flooding; e.g., the 2010-2012 La Niña event caused widespread flooding between September 2010 and March 2011 across all eastern states including Tasmania (cf. http://www.bom.gov.au/climate/enso/lnlist/). On the other hand, positive IOD events are linked to decreased inter-annual rainfall over northern and western Australia. Negative IOD enhances rainfall especially over the western part of the continent. More details of the role of ENSO and IOD in the Australian climate are provided in http://www.bom.gov.au/climate/.

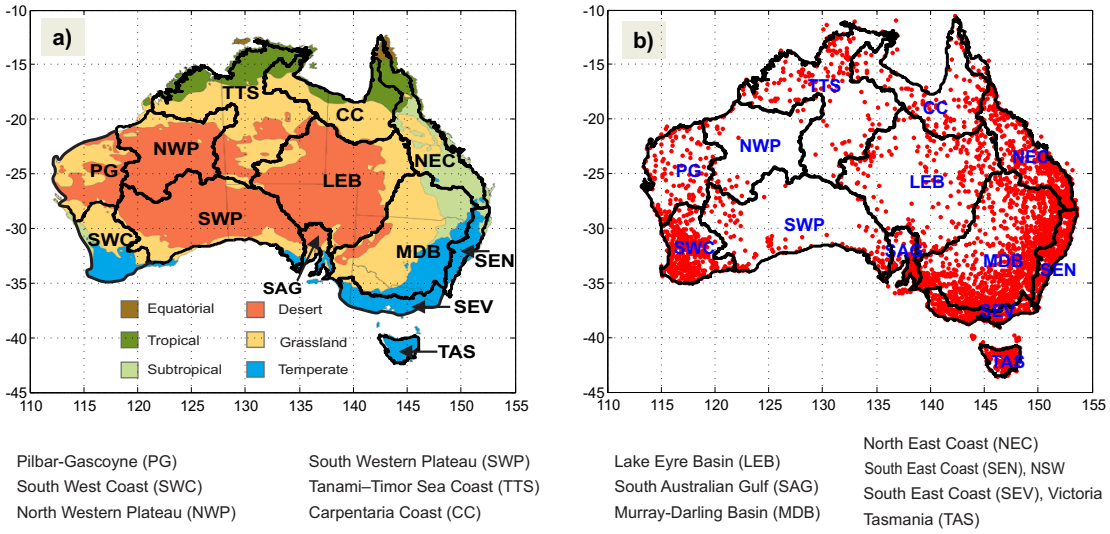

Figure 1: a) Six climate regions of Australia along with the 13 major river basins within the country. The climate regions are adapted from Stern et al. (2000) and the river basins are defined according to the drainage divisions and river regions provided by the Australian Bureau of Meteorology http://www.bom.gov.au/water/geofabric/inuse.shtml. b) Location of the in-situ rain gauge stations within 13 basins from the Bureau of Meteorology (BoM, Australia)

3. Data

3.1. Rainfall products

Daily estimates of rainfall at $0.05^\circ \times 0.05^\circ$ spatial resolution were provided by the Australian Bureau of Meteorology (BoM). These fields have been produced by interpolating rainfall observations from a relatively dense gauge networks across Australia using a sophisticated analysis technique (Jones et al., 2009). Monthly gridded rainfall products were computed here by averaging daily estimates covering 1981-2014.

Figure 1b shows the overall distribution of rain gauges across Australia contributing to the gridded rainfall analyses for the entire study period (1981-2014) consisting of about 3,800 rain gauges. About ~68% of stations contain data gaps of less than 10% over the entire period of study. Although gauge distribution is relatively dense across much of Australia, vast arid regions in the interior have few gauges (Figure 1b). Such data gaps result in uncertain interpolation estimates, and care was taken when interpreting results in basin-average analysis.

Other datasets used in this study include two satellite-based precipitation products and two reanalysis products:

a) TMPA version 7: The Tropical Rainfall Measuring Mission (TRMM) Multi-satellite Precipitation Analysis (TMPA, Huffman et al., 2007) provides near-global high-resolution ($0.25^\circ \times 0.25^\circ$) precipitation estimates both in real-time and as post-processed data after incorporating gauge data. Monthly TMPA version 7 (or known as TRMM 3B43 version 7) products, which are combined with monthly

gauge-based precipitation analyses from the Global Precipitation Climatology Center (GPCC, Schneider et al. , 2014, http://precip.gsfc.nasa.gov/), were used for the period 1998-2014. The TMPA version 7 products used here may be different from version 6, which has been used in most previous analyses. For an evaluation of TRMM products over Australia see e.g., Fleming and Awange (2013).

b) CHIRP: The US Geological Survey (USGS) in collaboration with the US Department of Interior (DOI) have recently developed a near-global very high-resolution ($0.05°\times0.05°$) infrared-based precipitation dataset known as the Climate Hazards Group InfraRed Precipitation (CHIRP, Funk et al., 2014). CHIRP is produced by integrating several long-term and short-term IR rainfall products (Funk et al., 2012). So far, this unique long-term satellite-only product has not been evaluated for Australia. In this study, monthly $0.05°\times0.05°$ products covering 1981 to 2014 (from `http://chg.geog.ucsb.edu/data/`) were used.

c) ERA-Interim: ERA Interim is a global atmospheric reanalysis produced by the European Center for Medium-Range Weather Forecasts (ECMWF, Dee et al., 2011). Several gridded products describing the ocean, land surface and atmospheric (covering the troposphere and stratosphere) conditions have been integrated to produce global fluxes at 3-hourly to 6-hourly time-scales with a spatial resolution of $\sim0.79°\times0.79°$. The Integrated Forecast System also produces precipitation forecasts, as the sum of stratiform (large-scale) and convective (small-scale) precipitation. The products were provided as precipitation rates (mm/hour) at 6-hourly intervals from 1979. Data for 1981-2014 were retrieved over the Australian continent from the ECMWF website (`http://apps.ecmwf.int/datasets/data/interim_full_daily/`).

d) MERRA: The Modern Retrospective Analysis for Research Application (MERRA, Rienecker et al., 2011) is an American global reanalysis for the satellite-era (1979 onwards) produced by the National Aeronautic and Space Administration (NASA, US) using the Goddard Earth Observing Data Assimilation System version 5 (GEOS-5). The retrospective analysis is performed at a relatively high spatial resolution ($0.67°\times0.50°$) at 1-hourly to 6-hourly time intervals, while focusing mainly on the assimilation of the global hydrological cycle by integrating a variety of satellite and surface observing systems. In this study, average monthly precipitation rates from the MERRA-Land data set (`http://gmao.gsfc.nasa.gov/research/merra/merra-land.php`) were used for 1981-2014.

The two reanalysis products mentioned above differ in many aspects, both in terms of the numerical modeling and observational data assimilation schemes (see, Dee et al., 2011; Rienecker et al., 2011, and references therein). For instance, a four-dimensional variational (4Dvar) scheme is used to correct biases in producing ERA-Interim products, whereas a 3Dvar scheme is used for the same purpose in MERRA (e.g., Bromwich et al., 2011). For Australia, Peña-Arancibia et al. (2013) reported that ERA-Interim represents rainfall seasonality in the southern and northern regions well in comparison with other reanalysis products. Conversely, the long-term trend in MERRA was reported to be more consistent with runoff observations and vegetation indices, see e.g., Los (2014).

The precipitation data used are summarized in Table 1. All data were averaged to a common grid of $0.50°\times0.50°$ and monthly time step to allow a consistent comparison. Otherwise the sampling error caused by spatio-temporal mismatch likely represents non-negligible impact on the final results. The ERA-Interim and MERRA needed to be downscaled to a finer spatial resolution, which was done by bilinear interpolation. A comparison between the spatial representation of BoM and the satellite/reanalysis products has been presented in the Appendix.

Table 1: Summary of the datasets used in this study.

Product	Type	Spatial Resolution [lat x lon]	Temporal Resolution	Coverage	Data used
BoM	Gauge-only	0.05° x 0.05°	Daily	Australia	1981-2014
TMPA	Satellite+gauge	0.25° x 0.25°	Monthly	50°S – 50°N	1998-2014
CHIRP	Satellite-only	0.05° x 0.05°	Monthly	50°S – 50°N	1981-2014
ERA-Interim	Reanalysis	0.79° x 0.79°	6-hourly	Global	1981-2014
MERRA	Reanalysis	0.67° x 0.50°	6-hourly	Global	1981-2014

3.2. ENSO and IOD indices

The strength of ENSO is commonly summarized in SST anomalies such as those within the Niño 3.4 region (5°N-5°S, 120°-170°W). ENSO events are said to occur if SST anomalies exceed ±4°C for 6 months or more (Trenberth, 1990). IOD is commonly measured by the difference between SST anomalies in the western (50°E-70°E and 10°S-10°N) and eastern (90°E-110°E and 10°S-0°S) equatorial Indian Ocean, which is referred to as Dipole Mode Index (DMI, Saji et al., 1999).

In this study, we used monthly Niño 3.4 ENSO index (time series from the Climate Prediction Center (http://www.cpc.ncep.noaa.gov/products/analysis_monitoring/ensostuff/) and for IOD, DMI index time series from the Low-latitude Climate Prediction Research (http://www.jamstec.go.jp/frsgc/research/d1/iod/e/iod/). The indices were provided as normal-standardized differences (Niño 3.4) or standardized differences (DMI) of SST anomalies in the equatorial Pacific and the Indian Ocean, respectively. The Niño 3.4 values were multiplied with -1 to make the sign consistent with the Southern oscillation Index (SOI) used by BoM, where positive values represent La Niña conditions and negative values El Niño events. For intuitive consistency, DMI was also multiplied with -1 (cf. Garćia-Garćia et al., 2011; Forootan et al., 2012) so that, similarly, positive and negative values relate to generally wetter and drier conditions, respectively. Index values bigger than 1 or smaller than −1 are likely related to strong ENSO/IOD events.

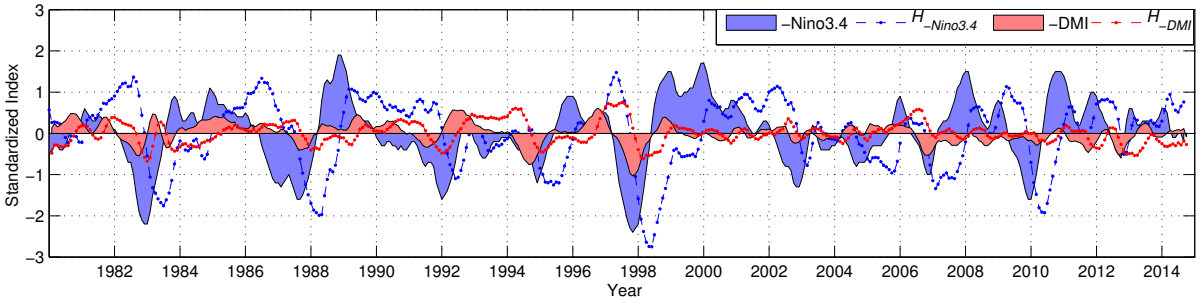

Figure 2: Monthly ENSO (-Niño 3.4) and IOD (-DMI) indices and their Hilbert transformed time series.

4. Method

4.1. Extracting the contribution of ENSO/IOD using MLR

In order to quantify the contribution of ENSO/IOD and to derive long-term and decadal changes/variabilities in monthly precipitation over Australia, the multi-linear regression (MLR) method was applied. Let us consider that $\mathbf{X}$ contains the time series of monthly rainfall anomalies over Australia, after removing their long-term temporal mean. For monthly 0.5°x0.5° precipitation grids over Australia covering the period 1981-2014, $\mathbf{X}_{n\times m}$ has the dimension of $n = 408$ and $m = 2908$, where n is the number of months and m represents the number of rainfall grid cells over the continent. Each entry of $\mathbf{X}$ is defined by $x(l, j)$, $l = 1, \ldots, n$, $j = 1, \ldots, m$. This notation is adhered to throughout, while time t is always represented in years. The MLR is then formulated as

$$\begin{aligned}\mathbf{X} = x(l,j) = \beta_1(j).t + \beta_2(j).\cos(2\pi t) + \beta_3(j).\sin(2\pi t) \\ +\beta_4(j).\cos(4\pi t) + \beta_5(j).\sin(4\pi t) + \\ \beta_6(j).N(t) + \beta_7(j).\mathcal{H}(N(t)) + \\ \beta_8(j).D(t) + \beta_9(j).\mathcal{H}(D(t)) + \epsilon(t),\end{aligned} \tag{1}$$

where $\beta_1(j)$ to $\beta_9(j)$ are coefficients, $N(t)$ and $D(t)$ the normalized -Niño 3.4 (ENSO) and -DMI (IOD) time series, and $\epsilon(t)$ random noise. The indices were shifted in the frequency domain by 90 degrees using Hilbert transformation ($\mathcal{H}(.)$, Horel, 1984) to capture the out of phase behavior of precipitation changes due to ENSO/IOD (see also, Phillips et al., 2012). The time series of -Niño 3.4 and -DMI as well as

their respective Hilbert transforms are shown in Figure 2.

The coefficients $\beta_{1..9}(j)$ were determined using a least squares adjustment (LSA). The adjusted coefficients ($\hat{\beta}_{1..9}(j)$) and their properties are summarized in Table 2, where $\hat{\beta}_1(j)$ represents the linear trend, $\hat{\beta}_2(j)$ and $\hat{\beta}_3(j)$ the mean annual variability, while that of semi-annual is contained in $\hat{\beta}_4(j)$ and $\hat{\beta}_5(j)$, the variability due to ENSO is captured by $\hat{\beta}_6(j)$ and $\hat{\beta}_7(j)$, and that of IOD by $\hat{\beta}_8(j)$ and $\hat{\beta}_9(j)$. The uncertainties of the adjusted coefficients were estimated following Brook and Arnold (1985) and Rieser et al. (2011). It should be mentioned here that the sinosuidal base functions that are used in Eq. 1 (to account for seasonality) might not be very suitable to adequately capture the complexity of the annual and semi-annual components of rainfall variability, whereby the frequency and the amplitude of seasonal cycles might change due to various climatic circulations over the continent (e.g., Drosdowsky, 1993). However, later in this paper we will show that such imperfect seasonality reduction does not significantly affect the extraction of the ENSO/IOD mode in rainfall records. The ENSO/IOD mode from the MLR technique (superindex 'MLR') can be computed from

$$\mathbf{X}^{\mathrm{MLR}}_{\mathrm{ENSO/IOD}} = x(l,j)^{\mathrm{MLR}}_{\mathrm{ENSO/IOD}} = \hat{\beta}_6(j).N(t) + \hat{\beta}_7(j).\mathcal{H}(N(t)) + \hat{\beta}_8(j).D(t) + \hat{\beta}_9(j).\mathcal{H}(D(t)), \quad (2)$$

while the non-ENSO/IOD mode (from MLR) was estimated as the total precipitation changes after removing Eq. 2 as

$$\mathbf{X}^{\mathrm{MLR}}_{\text{non-ENSO/IOD}} = x(l,j)^{\mathrm{MLR}}_{\text{non-ENSO/IOD}} = x(l,j) - x(l,j)^{\mathrm{MLR}}_{\mathrm{ENSO/IOD}}. \quad (3)$$

The non-ENSO/IOD mode in Eq. 3 contains the mean ('normal') seasonal changes, thus, no spectral information is lost through the performed ENSO/IOD and non-ENSO/IOD separation.

Table 2: Properties of the coefficients in Eq. 1. The coefficients $\hat{\beta}_1(j)$ to $\hat{\beta}_9(j)$ ($j = 1, \ldots, m$ being grid box indices) were determined using a least squares adjustment (LSA).

	Linear rate [mm/yr]	
Trend	$\beta_1(j)$	
	Amplitude [mm/yr]	Phase [deg]
Annual cycle	$(\hat{\beta}_2(j)^2 + \hat{\beta}_3(j)^2)^{0.5}$	$180/\pi.\tan^{-1}(\hat{\beta}_3(j)/\hat{\beta}_2(j))$
Semi-annual cycle	$(\hat{\beta}_4(j)^2 + \hat{\beta}_5(j)^2)^{0.5}$	$180/\pi.\tan^{-1}(\hat{\beta}_5(j)/\hat{\beta}_4(j))$
ENSO contribution	$(\hat{\beta}_6(j)^2 + \hat{\beta}_7(j)^2)^{0.5}$	$180/\pi.\tan^{-1}(\hat{\beta}_7(j)/\hat{\beta}_6(j))$
IOD contribution	$(\hat{\beta}_8(j)^2 + \hat{\beta}_9(j)^2)^{0.5}$	$180/\pi.\tan^{-1}(\hat{\beta}_9(j)/\hat{\beta}_8(j))$

4.2. Extracting the contribution of ENSO/IOD using CEOF

CEOF is a statistical technique alternative to principal component analysis (PCA, Preisendorfer, 1988) and allows extraction of non-stationary patterns from time series (Horel, 1984). CEOF is of interest here because ENSO/IOD represents a dynamic impact (changing in space and time) on precipitation changes over the continent. Unlike the MLR technique (Section 4.1), no pre-defined patterns for ENSO/IOD need to be assumed. Instead, the ENSO/IOD contribution in precipitation was statistically extracted as the first two dominant modes of the CEOF analysis. To perform CEOF, first the mean annual and semi-annual cycles were removed from each rainfall time series using

$$\mathbf{X}_{\text{non-seasonal}} = x(l,j)_{\text{non-seasonal}} = x(l,j) - (\hat{\beta}_2(j).\cos(2\pi t) + \hat{\beta}_3(j).\sin(2\pi t) + \hat{\beta}_4(j).\cos(4\pi t) + \hat{\beta}_5(j).\sin(4\pi t)), \quad (4)$$

where the coefficients $\hat{\beta}_2$ to $\hat{\beta}_5$ were estimated by fitting the MLR model of Eq. 1. A complex field was defined as $\mathbf{Y}$ containing the non-seasonal time series in Eq. 4 as its real part, and their Hilbert

transform (Horel, 1984) as the imaginary part:

$$\mathbf{Y}_{\text{non-seasonal}} = y(l,j)_{\text{non-seasonal}} = x(l,j)_{\text{non-seasonal}} + i\,\mathcal{H}\left(x(l,j)_{\text{non-seasonal}}\right), \tag{5}$$

where $i = \sqrt{-1}$. It follows that the real part of $\mathbf{Y}_{\text{non-seasonal}}$ equals $\mathbf{X}_{\text{non-seasonal}}$.

The generated complex dataset (Eq. 5) contains information about non-seasonal changes in rainfall and their temporal rate of changes as introduced by the Hilbert transform. Singular value decomposition (Preisendorfer, 1988) was applied to decompose the generated complex field as $\mathbf{Y}_{\text{non-seasonal}} = \mathbf{PE}^T$. This decomposition results in complex spatial patterns ($\mathbf{E}$), known as the complex empirical orthogonal functions (CEOFs), and the temporal patterns ($\mathbf{P}$) called the complex principal components (CPCs). Thus, both CEOFs and CPCs contain real and imaginary parts. The dominant modes of non-seasonal rainfall variability can be expressed using CEOFs and CPCs in terms of amplitude and phase (see e.g., Forootan, 2014, pages 32-36). The ENSO/IOD mode derived from CEOF analysis (superindex 'CEOF') can be reconstructed from the first two dominant CEOF modes as

$$\mathbf{X}^{\text{CEOF}}_{\text{ENSO/IOD}} = x(l,j)^{\text{CEOF}}_{\text{ENSO/IOD}} = \text{real}(\mathbf{P}(:,1:2)\mathbf{E}(:,1:2)^T), \tag{6}$$

while the non-ENSO/IOD mode can be calculated as the residual precipitation after removing the contribution derived via Eq. 6 as

$$\mathbf{X}^{\text{CEOF}}_{\text{non-ENSO/IOD}} = x(l,j)^{\text{CEOF}}_{\text{non-ENSO/IOD}} = x(l,j) - x(l,j)^{\text{CEOF}}_{\text{ENSO/IOD}}. \tag{7}$$

Therefore, similar to the MLR case (Eq. 3), the non-ENSO/IOD mode of rainfall variability in Eq. 7 contains the mean seasonal pattern estimated in Eq. 4.

5. Results

5.1. Seasonal rainfall variability

In order to explore the long-term (1981-2014) variability in rainfall over Australia, the MLR model of Eq. 1 was fitted to the time series of BoM products. Figures 3a and b show the spatial distribution of the seasonal variability over the entire period of study (1981-2014). The seasonal values, with the highest amplitudes of 250±18 mm/yr and 180±15 mm/yr respectively over the tropical northern Australia and along the southwest and east coast, were removed from rainfall time series to extract the ENSO/IOD mode.

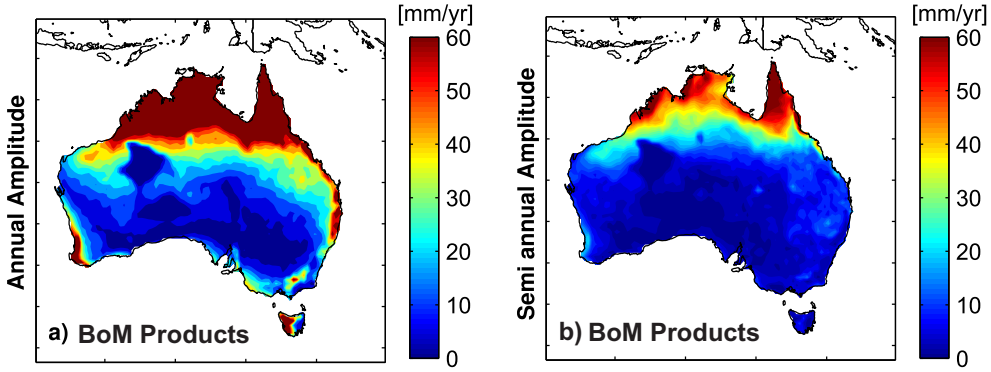

Figure 3: Annual (a) and semi-annual (b) amplitudes over Australia computed from long-term (1981-2014) rainfall dataset of BoM. The amplitudes are scaled between 0-60 mm/yr. Table 2 provides the formulations to estimate the maps.

With the growing number of global high-resolution precipitation products in the past two decades for regional applications, it is important that these precipitation datasets accurately represent the spatial and temporal aspects of rainfall variability over Australia. These not only include instantaneous hourly

to monthly continental rainfall but also must provide accurate and reliable representation of climate extremes and responses to major large-scale climate mechanisms such as ENSO and IOD. While satellite- and reanalysis-based rainfall estimates are being consistently evaluated to assess their hourly-to-daily rainfall frequency and detection (Chen et al., 2013; Peña-Arancibia et al., 2013) and monthly rainfall accumulations (e.g., Fleming and Awange, 2013), the continental long-term behavior has not widely been investigated. The spatial characteristics of TMPA, CHIRP, ERA-Interim and MERRA are compared with those of the BoM estimates in Appendix A, which suggests spatial correlation lengths for the CHIRP, ERA-Interim and TMPA products of $\sim 200 - 300$ km, comparable with those in the BoM estimates. Correlation lengths were slightly larger (~ 500 km) for MERRA.

The seasonal amplitudes of differences between the BoM estimates and the satellite and reanalysis estimates are shown in Figure 4. The results show that both TMPA (covering 1998-2014) and CHIRP (1981-2014) are in strong agreement with BoM estimates, except in the northwestern region where BoM estimates are unreliable (see Figure 4a and b for TMPA and Figure 4c and d for CHIRP). This was somewhat expected for TMPA (v7), which incorporates GPCC gauge observations. The differences between BoM and ERA-Interim or MERRA were greater than for satellite products. Significant underestimates of up to ~20 mm/year were found, particularly over the monsoonal northern part of the continent (see Figure 4e to h).

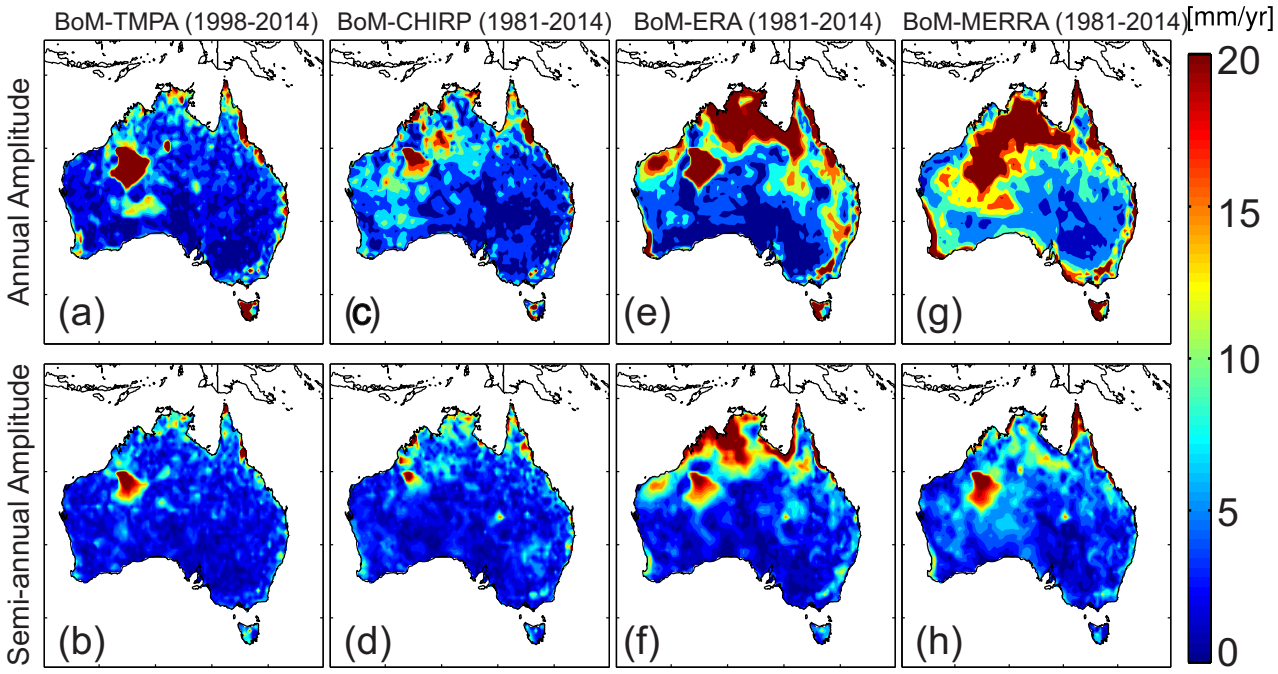

Figure 4: Amplitudes of annual and semi-annual differences between BoM and (a and b) TMPA product over 1998-2014, (c and d) CHIRP product over 1981-2014, (e and f) ERA-Interim product over 1981-2014, and (g and h) MERRA product over 1981-2014.

5.2. ENSO/IOD mode of rainfall from the MLR analysis of BoM products

The decadal and long-term patterns of ENSO and IOD amplitudes and their long-term phase propagation are shown in Figure 5. The amplitudes represent the quantitative contribution of each phenomenon to the total rainfall over Australia. A total of 14 weak to strong ENSO event (comprising nine El Niño and five La Niña phases) and 12 IOD event (eight positive and four negative phases) occurred during the past three decades (Figure 2, see also, `http://www.bom.gov.au/climate/`). Considerable inter-decadal variations in continental rainfall were associated to both ENSO and IOD during the past three decades.

At continental scale, the ENSO contribution to rainfall was found to be more dominant (∼12% of total rainfall) than IOD (∼7%). These values were estimated as averages of the ratios computed by dividing the amplitudes of ENSO (Figure 5a-d) and the amplitudes IOD (Figure 5f-i) by the total signal root-mean-squares (not shown). Compared to preceding decades, the contribution of ENSO was more prominent during 2001-2014 in the northern tropical region and in the eastern basins, in response to two moderate-strong La Niña events in 2007-2008 and 2010-2012 (compare Figure 5a-c). During 1981-1990 and 1991-2000, the IOD contribution was less prominent than ENSO but more distinguishable, due to two strong positive IOD events in 1994-1995 and 1997-1998. Larger values for IOD-derived inter-annual amplitudes were found for 2001-2014, coinciding with stronger ENSO activity in this decade (Figure 5h). The ENSO and IOD events as reflected in the respective indices are to some extent correlated, however. This may have had influence on the respective decadal amplitude estimates. The decadal correlation barely exceeded a (lag-zero) correlation coefficient of 0.25, however, and therefore was not explicitly considered in applying MLR.

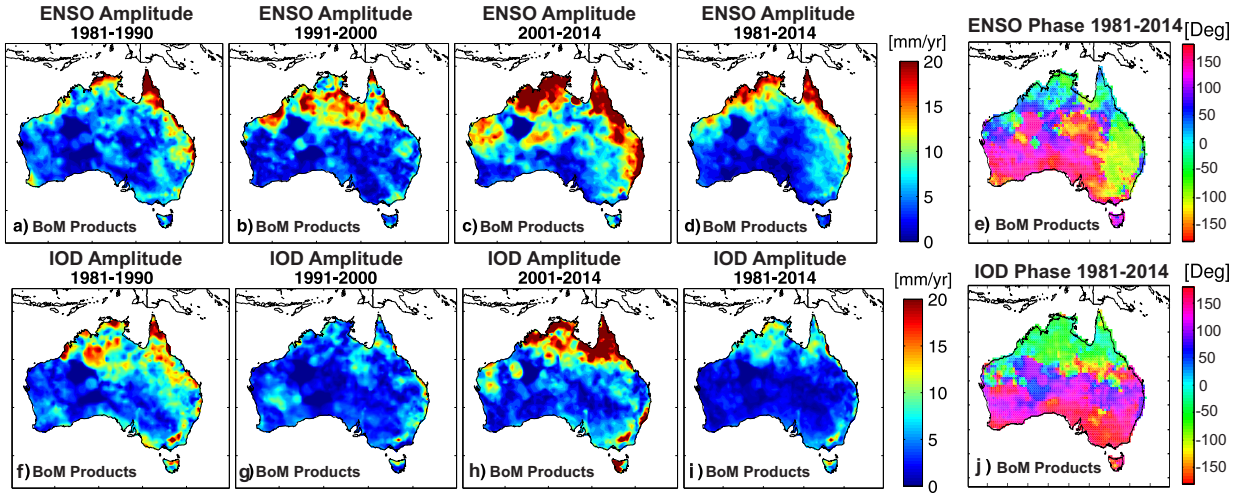

Figure 5: Amplitudes and phase propagation of ENSO/IOD mode over Australia for the decadal intervals and the long-term (between 1981 and 2014) computed using the MLR technique described in Section 4.1. Figures 5a, b, c, and d correspond to the amplitude of ENSO over 1981-1990, 1991-2000, 2001-2014, and 1981-2014, respectively. Figure 5e shows the phase propagation that corresponds to ENSO over 1981-2014. Figures 5f, g, h, and i correspond to the amplitude of IOD over 1981-1990, 1991-2000, 2001-2014, and 1981-2014, respectively. Figure 5j indicates the phase propagation of IOD over 1981-2014. The amplitudes and the two propagation patterns are estimated according to the formulations in Table 2. Temporal lags between the ENSO/IOD mode of rainfall variability and the indices are shown in Figure 10.

The long-term mean phase propagations of ENSO and IOD modes (Figures 5e and j, respectively) indicate that ENSO effects usually develop in the east (the North East Coast, South East Coast, and Murray-Darling basins) during autumn (cf., Cai et al., 2011) and IOD in the tropical north and south during spring.

Due to the hydro-climatic and economic significance of the drainage basins, the results were also expressed as basin averages. Average annual, semi-annual, ENSO, and IOD amplitudes of long-term precipitation for the 13 basins of Figure 1 are shown in Table 3. Substantial variations were found among basins, with the Carpentaria Coast (CC) showing the largest overall amplitude, followed by the Tanami-Timor Sea (TTS) and North East Coast (NEC). The South Western Plateau (SWP) showed the smallest amplitude and the least ENSO influence, while greatest ENSO influence was found in the northern and eastern basins. For 1981-2014, the highest IOD amplitudes were found over Tasmania (8.1±6.5 mm/year), CC (6.3±8.4 mm/year), and TTS (5.8±6.5 mm/year).

5.3. ENSO/IOD- and non-ENSO/IOD modes of rainfall from CEOF

Before applying CEOF, a 5-month moving average filter was applied to the monthly non-seasonal rainfall anomalies to filter out high-frequency temporal variability of rainfall. The signal dampening due

Table 3: Average amplitudes of rainfall over various rivers basins (see Figure 1) across Australia computed using BoM products over the period 1981-2014. For the locations and abbreviations of the basins, see Figure 1

Basin	CC	TTS	NEC	SEN	NWP	PG	SWC	SWP	SAG	LEB	MDB	SEV	TAS
Area (km^2)	631,893	1,154,262	447,937	129,574	715,794	477,240	326,032	1,093,049	113,281	1,308,429	1,062,025	134,336	64,136
	Amplitudes in mm/yr												
Annual	101.3±10.7	79.4±8.3	62.2±9.2	34.4±9.7	27.1±4.4	17.3±5.3	22.6±3.6	4.5±2.6	8±3.3	16±4.3	6.2±4.5	18.3±4.5	41.2±8.3
Semi-annual	45.2±10.5	31.3±8.2	18.6±9.1	1.5±9.6	12.4±4.3	10.8±5.2	6.4±3.6	1.5±2.5	2.3±3.3	5.7±4.3	6.1±4.5	2.7±4.4	0.5±8.2
ENSO	9.6±8.2	8.8±6.3	12.1±7.1	8.8±7.4	4.2±3.3	6.4±4.1	2.7±2.8	1.2±2	0.8±2.6	2.9±3.3	5.4±3.5	2.2±3.5	1.9±6.4
IOD	6.3±8.4	5.8±6.5	2±7.2	4.5±7.6	1.4±3.4	1.3±4.2	1.3±2.9	1.7±2	4±2.6	1±3.4	2.3±3.6	5.4±3.5	8.1±6.5

to the application of the filter was accounted for by simulating seasonal time series (according to Eq. 1) and applying the same 5-month moving average filter. Scaling factors were computed as ratios of the original time series and the filtered values. The filtered time series were then multiplied by the estimated scales.

Filtered (and scaled) time series were then transformed to include the phase shifted values using Eq. 5. Following Horel (1984), the first and last 5 months were removed before applying CEOF decomposition to account for the artifacts introduced by the Hilbert transform. The CEOF technique was expected to be more efficient than the ordinary EOF analysis to extract ENSO/IOD contributions because of their non-stationary behavior (Figure 5). A comparison of CEOF and PCA for extracting the ENSO/IOD patterns was also performed, the results of which indicated that the patterns extracted by CEOF were better correlated with ENSO/IOD indices (not shown). The first two leading modes of CEOF, accounting for ∼29% and ∼14% of the total non-seasonal rainfall variability, are interpreted here because of their dominance and relevance to the ENSO and IOD patterns. The remaining ∼57% of non-seasonal variability mostly represents local precipitation distribution patterns.

Figure 6 presents the spatial patterns (real part of the first two dominant CEOF modes) of rainfall variability over Australia, with their corresponding temporal evolution shown in Figure 7. For brevity, the imaginary part of the spatial patterns is not shown. This does not however mean that the imaginary components are not important, while they represent the propagative behavior of rainfall variability over the continent. The two CEOF modes (Figures 6 and 7) represented the combined influence of ENSO and IOD indicating maximum precipitation over the tropical northern Australia (Figure 6a) and eastern Australia (Figure 6b). Rainfall over much of the northern and western Australia, and southern Tasmania exhibited the influence of IOD, while that of northern and eastern states exhibited the influence of ENSO. Their corresponding temporal patterns (real and imaginary PCs in Figure 7) were found to be correlated with ENSO (-Niño 3.4) and IOD (-DMI). The real part of the first complex PC was correlated to -Niño 3.4 (0.40 at lag of 1 month) while the correlation with -DMI was smaller (0.24 at a lag of 1 month). Higher correlation was found between the imaginary part of the first complex PC and -Niño 3.4 (0.43 at a lag of 1 month). The real and imaginary part of the second complex PC was found to be more correlated with -DMI (0.34 and 0.28 at a lag of 1 month, respectively). As is clear from the temporal evolution, the temporal patterns of Niño 3.4 and DMI are not fully reflected in the rainfall time series. Therefore, application of CEOF is likely better suited than MLR to extract the ENSO/IOD and non-ENSO/IOD modes.

The influence of ENSO/IOD on Australia rainfall are further supported by the power spectral density plots in Figure 8, where those of the first two real PCs were compared in the frequency domain with -Niño 3.4 and -DMI time series. Power spectral density plots were estimated using least squares spectral analysis (Vanicék, 1969) and the significance of the estimates was tested using the Fisher test as in Sharifi et al. (2013). The results indicate that ENSO corresponds better with the extracted rainfall modes given that the high peaks of -Niño 3.4 (at 0.08, 0.18, and 0.58 cycle/year) were also found in the spectrum of PC1 (Figure 8a). The highest peaks of PC2 were found to be similar to the frequency of 0.08 cycle/year from -Niño 3.4 and 0.33 cycle/year from -DMI (Figure 8b). Given that ENSO and IOD modes were significantly related to PC1 and and PC2, both CEOF modes appear to represent ENSO/IOD-induced rainfall anomalies. As it is clear from the spectral density plots, estimated for the two indices and the dominant PCs, the contribution of the annual and semi-annual variability in the ENSO/IOD mode is very minor (compared to other frequencies). Besides, the ENSO/IOD mode of rainfall variability for the period 1981-2014 was reconstructed by inserting the spatial patterns of Figure 6 (and the imaginary parts that are not shown here) and their corresponding temporal patterns

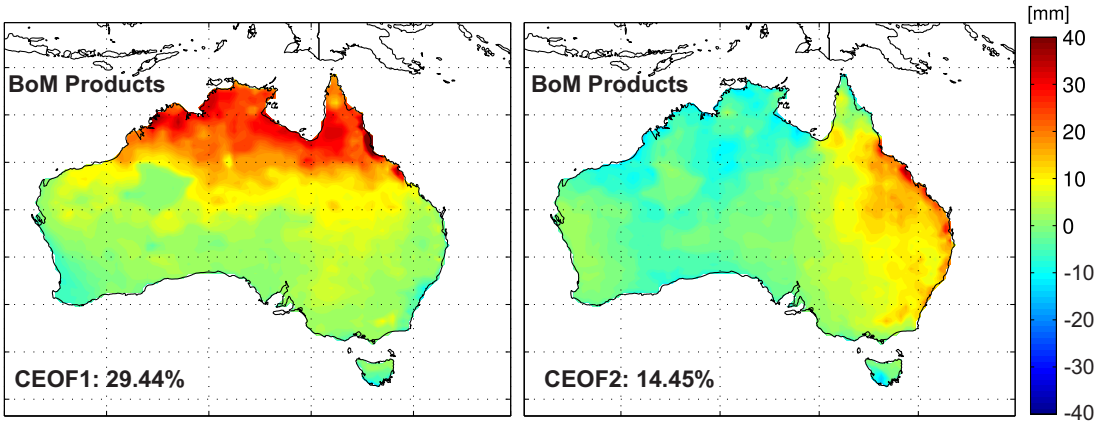

Figure 6: The real part of the first two leading CEOF modes of rainfall variability over Australia computed using the CEOF analysis of BoM products for the period 1981-2014. (a) represents the real part of the first spatial pattern, and (b) represents the real part of the second spatial pattern. The corresponding temporal patterns are shown in Figure 7.

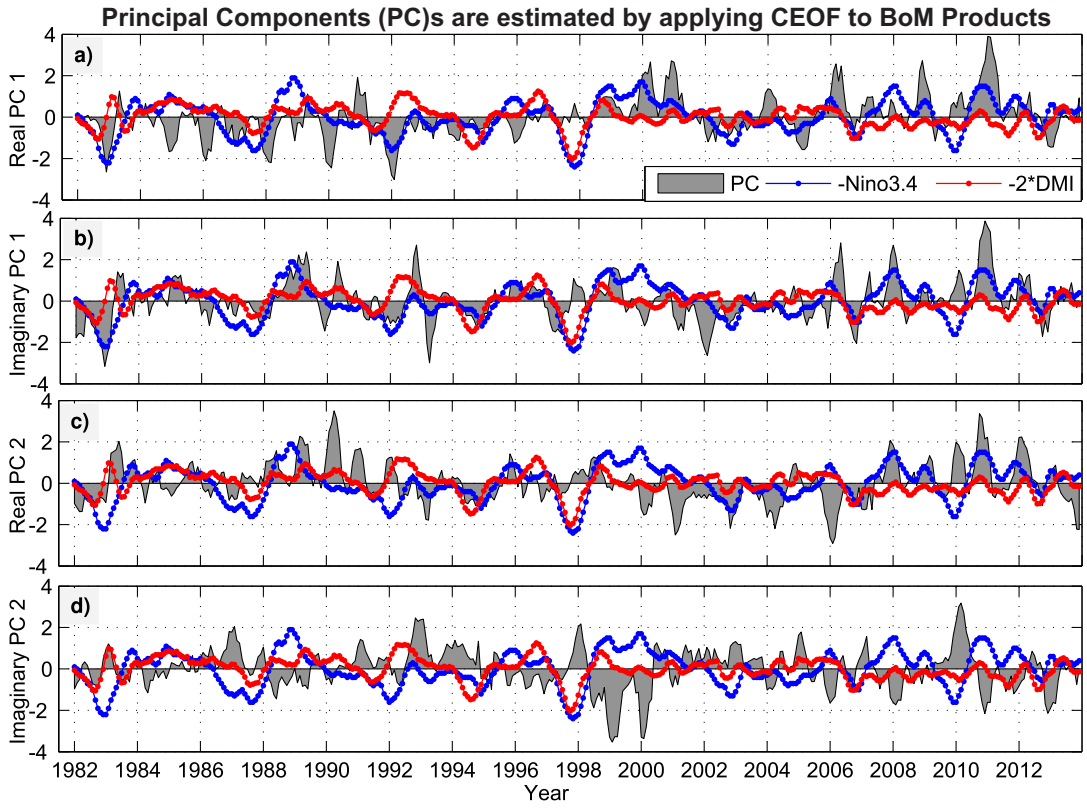

Figure 7: The complex principal components (real and imaginary parts of CPCs) corresponding to the first two leading modes of CEOFs computed using BoM datasets over the period 1981-2014. (a) and (b) respectively represent the real and imaginary part of the first mode, while (c) and (d) represent the real and imaginary part of the second mode, respectively.

(Figure 7) in Eq. 6. The standard deviations of the ENSO/IOD rainfall is shown in Figure 9. The largest variations (up to 50 mm/month) were found in the tropical north and the northeast (Figures 5 and 6). We found that the annual and semi-annual amplitudes of the ENSO/IOD mode reach up to 3 and 0.3 mm/year over 1981-2014, respectively (results are not shown). The estimated amplitudes are negligible compared to the magnitude of the ENSO/IOD mode (∼50 mm/year, see Figure 9) or the

seasonal amplitude of precipitation (∼150 mm/year, see Figure 3).

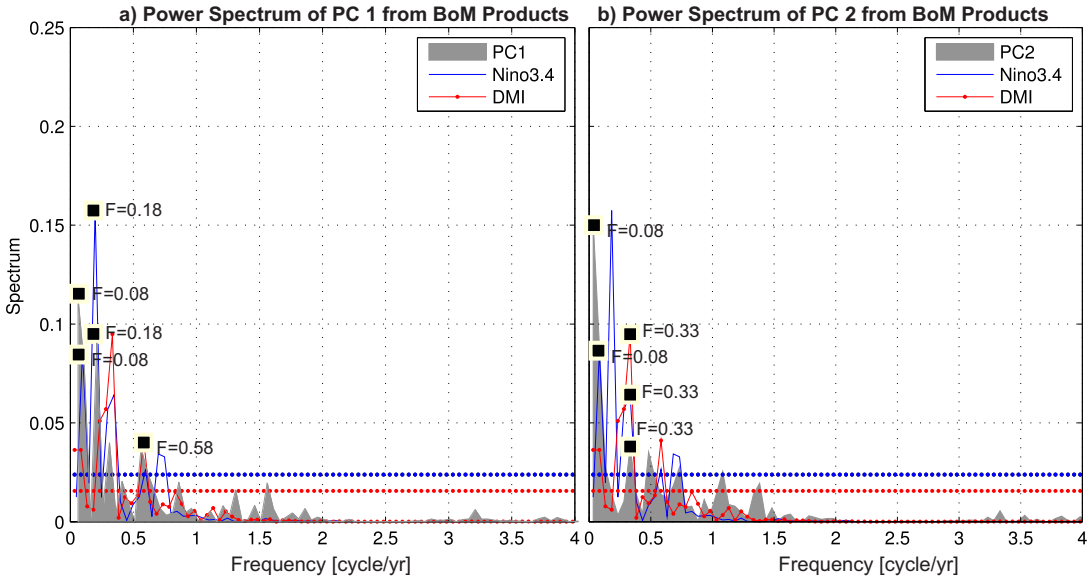

Figure 8: Power spectrum of the first two dominant temporal evolutions (PCs) of BoM rainfall data. Graphs also contain the power spectrum computed by considering the temporal patterns of -Niño 3.4 and -DMI representing ENSO and IOD events, respectively.

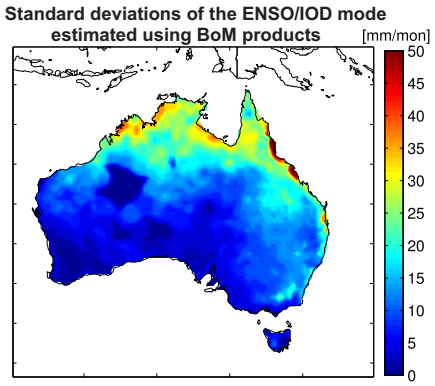

Figure 9: Standard deviations of the ENSO/IOD mode of Australian rainfall over the period 1981-2014 derived from CEOF analysis of BoM products.

Figure 10 shows the temporal correlation patterns between the ENSO/IOD mode of Australian rainfall and -Niño 3.4/-DMI over the entire period of 1981 to 2014. A two-tailed test (Best and Roberts, 1975) was applied to examine the significance of correlations. Low correlations (<0.18) were masked.

Correlations between -Niño 3.4 and the non-ENSO/IOD mode of rainfall were positive with the strongest relationship over the tropical north, west coast, and eastern regions of the continent (see Figure 10a) with a maximum correlation of 0.6 over the north and northwest. A maximum lag of up to 4 months was found over the Murray-Darling basin (MDB), while the rest of the continent experienced an almost instant influence of ENSO (Figure 10b). The rainfall-ENSO relationship was previously found to be partly associated with the inter-decadal fluctuation of atmospheric pressure over the northern

Pacific Ocean referred to as the Inter-decadal Pacific Oscillation (IPO) (Power et al., 1999; Risbey et al., 2009). Correlations were found to be stronger during the negative IPO phase (corresponding to the lower SST anomalies over the northern Pacific ocean), thus, favoring stronger correlations during the La Niña conditions. However, the notion of IPO as an independent climate mode has been questioned by Newman et al. (2003).

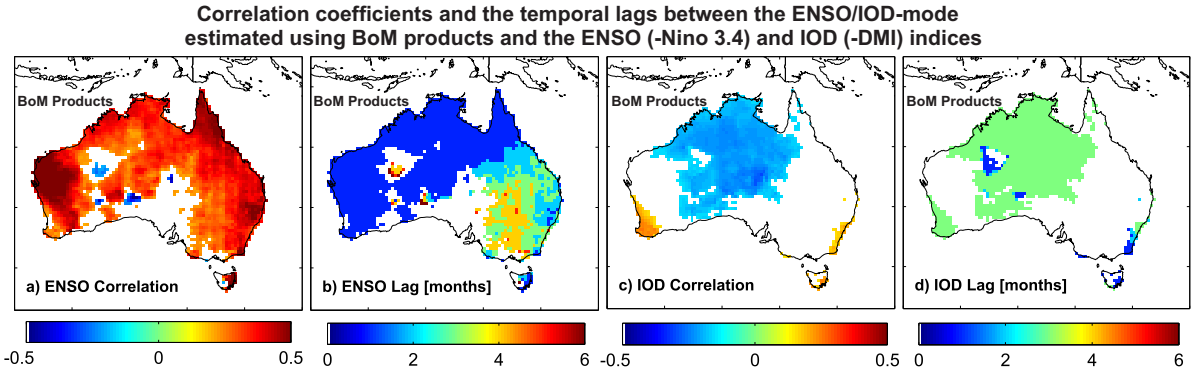

Figure 10: Correlation and lags between ENSO (-Niño 3.4 index) and IOD (-DMI index) and Australian rainfall (derived from BoM) for the period 1981-2014.

IOD correlations showed two contrasting patterns: (a) positive correlation (up to 0.32) over southwest and southeast including Tasmania (see Figure 10c) consistent with the results of Ashok et al. (2003a) and (Risbey et al., 2009) and (b) negative correlations (up to -0.30) over central and northern parts of Australia. While the correlations are not very strong over Australia, intense negative IOD events have resulted in widespread rainfall deficits over the southwest and southern Australia (e.g., Ashok et al., 2003a). Lags of up to 3 month were found between -DMI and the ENSO/IOD mode of rainfall variability over Australia (see Figure 10d). Although IOD events are known to occur independently of ENSO such as in 1994 (Ashok et al., 2003b), positive (negative) IOD events co-evolve with El Niño (La Niña) conditions, especially during spring (SON) (Figure 2) leading to extreme droughts (floods) over southern and eastern Australia (see, e.g., Ummenhofer et al., 2009b; Cai and Rensch, 2012; van Dijk et al., 2013).

Figure 11 shows both decadal (1981-1990, 1991-2000, and 2001-2014) and long-term (1981-2014) trends in rainfall over Australia. These decades were chosen to be consistent with previous (hydro-) climate studies, but it is noted that they do not necessarily coincide with change points in rainfall trends. A more sophisticated trend analysis was performed by Fu et al. (2010). The grid presentation was chosen in Figure 11 to show changes as detailed as possible. One can perform such analysis based on climatic regions or particular river basins. Trends in the total amount of rainfall were computed using Eq. 1 but omitting the last four ENSO/IOD related terms (Figure 11a-d). To estimate the trend of the ENSO/IOD and non-ENSO/IOD rainfall contributions separately the same regression was applied to the outputs of Eqs. 6 and 7 (Figures 11e to h and i to l, respectively).

Considerable variability was found in decadal total rainfall trends during the past three decades (Figure 11a to d). A significant influence of ENSO and IOD events is evident (Figure 11e-g). The spatial patterns of total precipitation changes for the period 1981-1990 (Figure 11a) indicate a decreasing trend (up to 4.5 mm/year) over tropical Northern Australia with a modest increase in ENSO/IOD-related rainfall (Figure 11e). An increase in ENSO/IOD-related rainfall trend was also found over eastern Australia despite the two major El Niño events in the 1980s (in 1982 and 1987). Linear trends during the last two decades (1991-2014) mainly suggested increases (up to 4 mm/year) (Figure 11b), leading to an overall rainfall increase (Figure 11d) for the period 1981-2014.

Decreasing rainfall trends were mainly observed over the southern Australia including Tasmania in the 1990s (Figure 11b), and over western Australia during the last decade (Figure 11c), which may be related to the influence of a strong southern annular mode (Nicholls, 2010), as well as weakening monsoon troughs over northern Australia during austral summer (December-January-February, Taschetto and England,

2009). Increases in long-term and decadal rainfall trends were influenced by higher rainfall as a result of moderate-strong La Niña events at the end of the decade (e.g., in 2011-2012). Besides increasing rainfall over Australia, decreasing trends were observed at the same time over northern, eastern and southern Australia (see, Figure 11i-k), which cannot be explained by ENSO/IOD. The long-term (1981 to 2014) trend in rainfall was dominated by ENSO/IOD (Figure 11h) during the last 10 years with almost no trend in non-ENSO/IOD rainfall over Australia. Increasing trends (Figure 11d) over the north, northwest, and western Tasmania and decreasing trends over the southwest and east coast of Queensland were consistent with previous findings (see, e.g., Nicholls et al., 1997; Smith, 2004; Nicholls, 2006; Taschetto and England, 2009; Li et al., 2013).

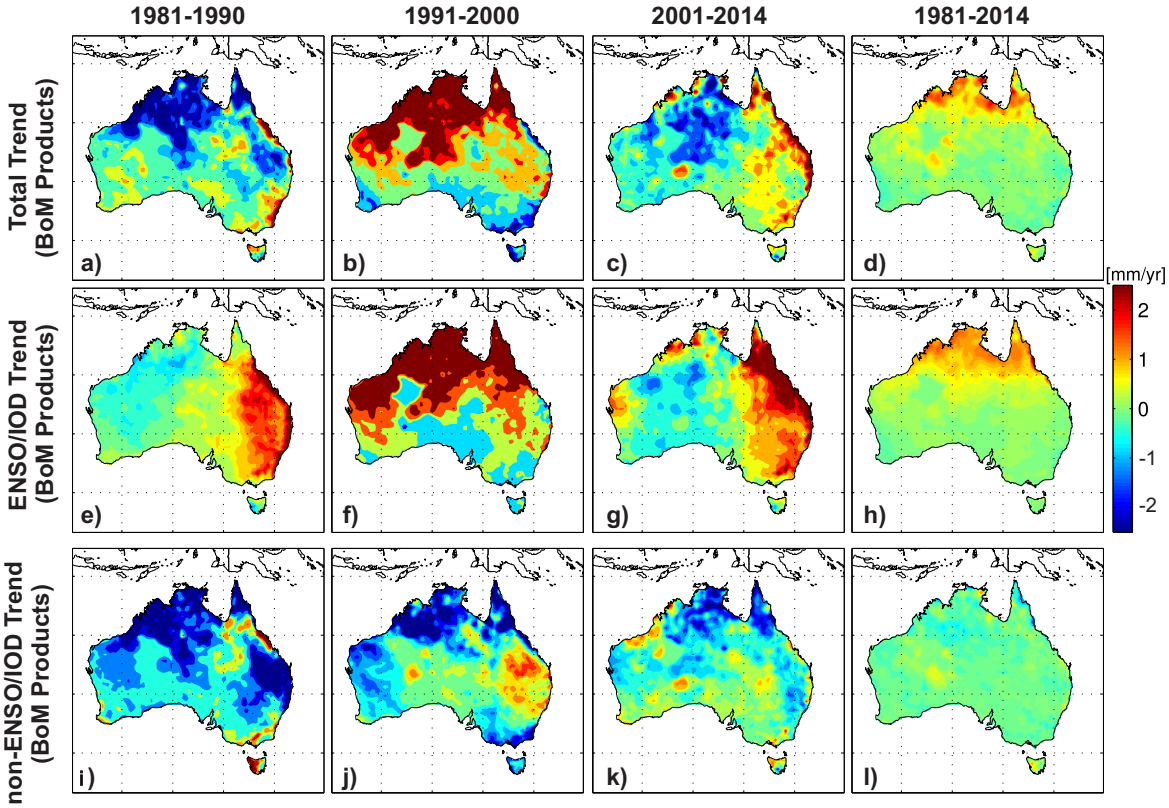

Figure 11: Decadal (1981-1990, 1991-2000, and 2001-2014) and Long-term (1981-2014) linear trends in Australia rainfall. (a-d) represent the total rainfall, (e-h) indicate trends in the ENSO/IOD mode, and (i-l) represent trends in the non-ENSO/IOD mode.

Although ENSO/IOD are the leading atmospheric drivers of inter-annual variability of rainfall over Australia, other factors such as Madden Jullian Oscillation (MJO, e.g., Wheeler et al., 2009), Southern Annular Mode (SAM, e.g., Hendon et al., 2007; Nicholls, 2010), and atmospheric blocking (e.g., Pook et al., 2013, and references therein) and their interaction with ENSO/IOD have been reported to produce substantial intra-seasonal rainfall variability across various parts of the continent (detailed discussion can be found in Risbey et al. (2009)). Because ENSO and IOD themselves are highly correlated in time, for example, during the austral spring (e.g., Ashok et al., 2003b; Risbey et al., 2009; Cai et al., 2011), the CEOF technique was not able to separate their independent contributions but the combinations of ENSO and IOD in the two modes were extracted successfully. We confirmed this by computing the correlations of the non-ENSO/IOD mode with -Niño 3.4 and -DMI indices; residual correlations were less than 0.25.

The decadal and long-term impact of ENSO and IOD varies across Australia as shown in Figures 9, 10, and 11 with compounding implications on hydrology including extreme events - droughts and floods. In an effort to quantify the impacts of ENSO/IOD on hydrology, the basin-averaged seasonal rainfall

(in km^3/month) between 1981 and 2014 was plotted for the 13 basins in Figure 12. The mean seasonal rainfall over various basins were found to be consistent with the correlation patterns shown in Figure 10, indicating greater impact of ENSO/IOD over the basins in the northern and eastern Australia including the Carpentaria Coast (CC) (Figure 12a), TTS (Figure 12b), NEC and South East Coast (Figure 12c-d), Lake Eyre Basin and South Australian Gulf (LEB and SAG, Figure 12i-j), as well as Murray-Darling Basin (MDB) and South East Coast (SEV) (Figure 12k-l). The highest rainfall was recorded in TTS followed by CC and NEC, while the lowest rainfall was observed over Tasmania and the South West Coast (SWC) basin, in which the ENSO/IOD impact was relatively small.

ENSO/IOD impacts appeared to occur in all river basins with continuous negative anomalies during the major drought conditions in the late 1990s and early 2000s for PG, SWC, SWP LEB, and MDB (see, e.g., Ummenhofer et al., 2009a; van Dijk et al., 2013). Anomalously high rainfall contributions were found due to the two successive La Niña events over the north (CC and TT), northwest (NWP), and east (NEC, LEB, and MDB basins) between 2010 and 2012. The last two events caused severe floods over northern and eastern Australia including eastern Tasmania (`http://www.bom.gov.au/climate/enso/lnlist/`). Table 4 reports the estimated linear trend in rainfall for all the river basins during the last three decades. With the exception of the Southwest Coast (SWC), all basins show increasing rainfall trends between 1981 and 2014, with significant trends in ENSO/IOD-related rainfall for most (CC, NEC, TTS, NWP, PG, SWP, and LEB). The decreasing rainfall trend over SWC has been reported previously (e.g., Nicholls, 2010) and has been attributed to the strong influence of the Southern Annular Mode over recent decades. Although ENSO/IOD events play a major role over MDB, no significant increasing trends were found during the period 1981-2014. In general, non-ENSO/IOD rainfall trends were found to be negative across the majority of basins (see also, Figure 11l) but the values were not statistically significant.

Table 4: Seasonal trends (in km^3/decade) in total rainfall volume over various rivers basins in Australia for the period 1981-2014. Please note that unlike Table 3, volumes of rainfall changes have been reported here. The overall uncertainties in the trend estimates were less than 1 mm/decade and were not shown here.

Basin	CC	TTS	NEC	SEN	NWP	PG	SWC	SWP	SAG	LEB	MDB	SEV	TAS
Total	7.3	10.1	2.6	0.0	2.7	1.0	0.0	1.9	0.0	2.4	0.0	0.0	0.0
ENSO/IOD	**5.9**	**9.3**	**2.2**	0.0	**2.0**	1.2	0.0	**1.4**	0.0	**3.0**	1.0	0.0	0.0

5.4. Evaluation of non-seasonal variations and trends in satellite and reanalysis products

In order to assess the skill of the satellite and reanalysis products in representing non-seasonal rainfall variability over Australia, their differences with BoM products after removing the annual and semi-annual cycles were assessed during the main four climate seasons. At the continental scale, the differences were found to be mainly over tropical northern Australia (similar to the seasonal differences in Figure 4) with TMPA, ERA and MERRA overestimating monthly rainfall and the IR-derived CHIRP underestimating rainfall, in both cases by more than 60 mm/month (not shown). Substantial underestimation also occurred along the coastal regions of southwest and eastern Tasmania.

Table 5 reports the non-seasonal root-mean-square-errors (RMSEs) of the three long-term (1981-2014) precipitation products for the 13 major river basins of Australia in comparison to BoM estimates. The RMSE values were calculated after removing the annual and semi-annual cycles with the aim of quantifying ~~the~~ uncertainties due to the influence of inter-annual changes as well as ENSO and IOD variability over the mentioned river basins. The estimated RMSEs were generally larger during the wet seasons (December to March) in the high rainfall regions of tropical northern Australia, e.g., Carpentaria Coast (CC), Tanami-Timor Sea Coast (TTS), and North East Coast (NEC) while precipitation errors were smaller in the other basins. Among the three precipitation products, MERRA indicated smaller RMSE than ERA-Interim and CHIRP for all the seasons. Anomalously large errors were found in ERA-Interim from September to May in the tropical north while it was found to be better than CHIRP during the JJA season for majority of the river basins (see, Table 5). While the magnitude of errors was found to be reduced substantially in ERA-Interim re-analysis over northern Australia during the TRMM-era (1998-2014, Table 6), the error magnitudes increased slightly in the central and southern river basins for the other two products, namely CHIRP and MERRA (e.g., LEB and MDB). TMPA precipitation

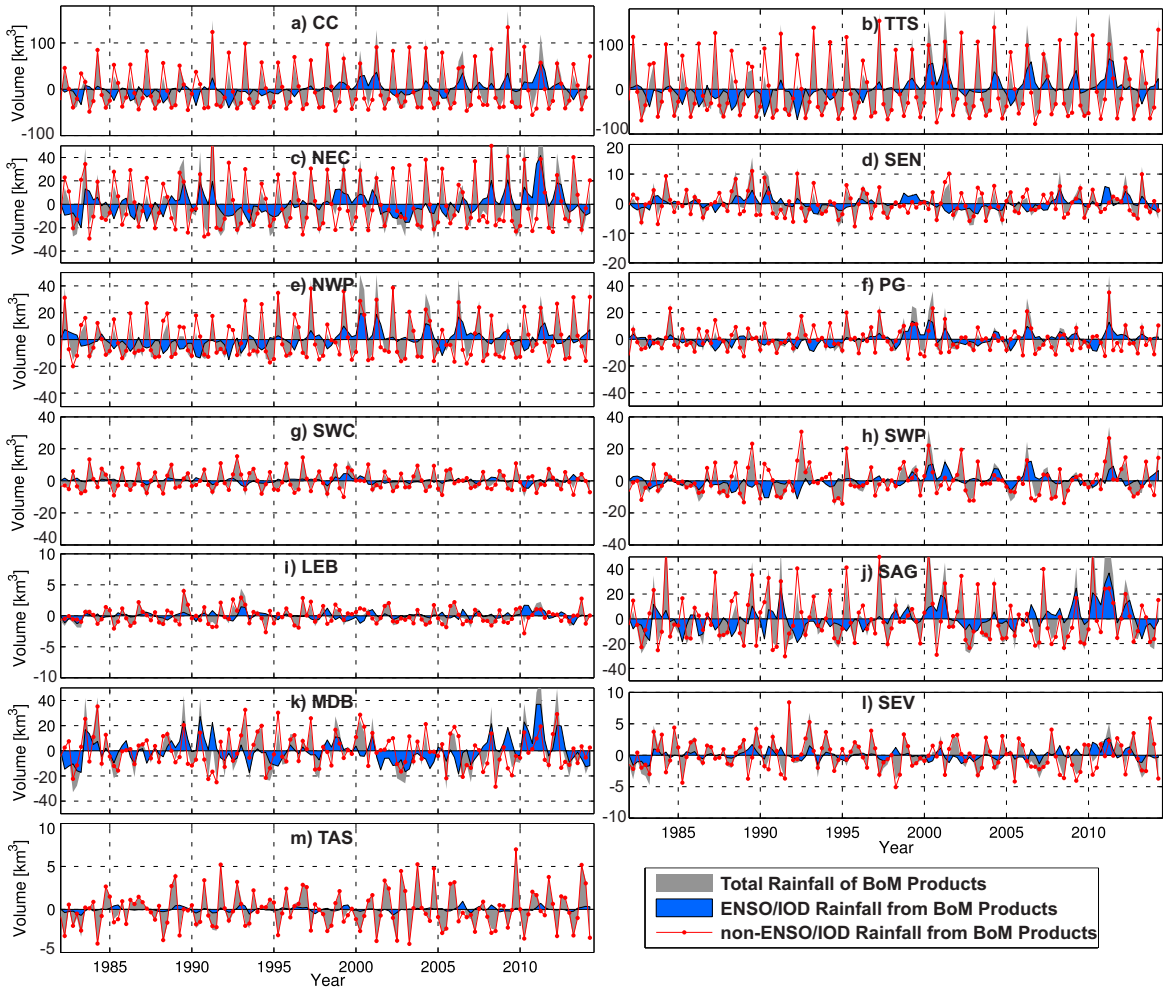

Figure 12: Basin-averaged seasonal rainfall variability between 1981 and 2014 computed based on BoM products. For estimating basin averages the boundaries of the 13 major river basins of Figure 1 were used. The values are expressed in volumes (in km^3/month) of accumulated rainfall, which were estimated by considering the areas of Table 3.

estimates were found to be comparable to MERRA and was relatively better than CHIRP for all the seasons with few exceptions (see, Table 6).

To compare the long-term behavior of precipitation over Australia, linear trends were computed using the satellite and reanalysis products. Computations were carried out based on basin averages of all 13 river basins during the period 1981-2014 (1998 to 2014 for TMPA). Table 7 reports the trend estimates from total precipitation and the trends due to ENSO/IOD rainfall. While there has been an increase in the amount of average rainfall over the majority of basins based on the observed rainfall datasets from BoM (see, Table 4 and 7), only CHIRP and MERRA were able to produce consistent trends, while ERA-Interim (1981-2014) and TMPA (1998-2014) showed negative trends for most basins. In fact, MERRA shows the most consistent trend estimates for all the basins (except for those of MDB and SEN), and trends in CHIRP precipitation products were found to be insignificant for both total precipitation and ENSO/IOD contributions. The magnitude of rainfall changes was also found to be quite consistent across all the long-term precipitation products (CHIRP, MERRA and ERA) with the SWC and Tasmania basins indicating no trend in both total precipitation and ENSO/IOD rainfall. This suggests that the CHIRP and MERRA precipitation products may be more suitable for estimating long-term rainfall trends over Australia, and specifically in representing the recent La Niña events (e.g., that

Table 5: Basin averaged RMSE of three long-term (1981-2014) precipitation products with respect to BoM datasets after removing the annual and semi-annual cycles.

BASIN	**CHIRP [mm/month] 1981-2014**				**ERA [mm/month] 1981-2014**				**MERRA [mm/month] 1981-2014**			
	DJF	MAM	JJA	SON	DJF	MAM	JJA	SON	DJF	MAM	JJA	SON
CC	16.4	12.8	5.6	8.8	39.7	20.6	4.4	18.7	10.3	6.6	2.7	5.1
TTS	15.2	11	4.3	7	40.6	21.7	4.3	23.7	12.1	6.4	1.9	6
NEC	14.4	14.1	9.4	11.8	16.9	8.4	3.5	10.1	8.6	8.2	3.7	5
SEN	13.7	12.6	9.1	9.8	9.9	9.6	4.5	13.2	6.9	5.8	3.2	3.9
NWP	7.9	6.7	2.9	3.7	16.6	9.9	2.3	5.8	11.1	6.9	1.9	5.1
PG	11.5	8.5	4.2	5.2	11.1	7.6	2.1	7.9	4.5	4	1.9	2.3
SWC	5.9	4.7	2.9	2.8	3.8	3.6	1.4	4.5	2.3	2.1	1.3	1.6
SWP	6.2	5	1.2	1.9	5.6	4	1.2	3	2.2	1.7	0.6	1
SAG	5.4	4.7	2.9	3.2	5.4	4.9	1.4	5.4	3.6	3.1	1.4	1.9
LEB	8.4	6	3.1	5.2	11	4.9	1.2	5.7	3.2	2.1	1.2	1.7
MDB	9.8	8.4	5.3	7.6	6.7	4.3	1.9	6.5	4.6	3.9	2.1	2.9
SEV	7	5.3	3.0	4.7	6.0	4.4	2.0	7.5	5.0	4.2	1.6	2.4
TAS	4.5	3.1	2.3	3.1	4.9	4.1	2.9	13.1	4.8	3.9	1.6	2.4

Table 6: Basin averaged RMSE of four precipitation products with respect to BoM datasets over 1998-2014. The RMSEs were obtained in the same manner as in Table 5.

BASIN	**TMPA [mm/month] 1998-2014**				**CHIRP [mm/month] 1998-2014**				**ERA [mm/month] 1998-2014**				**MERRA [mm/month] 1998-2014**			
	DJF	MAM	JJA	OND	DJF	MAM	JJA	OND	DJF	MAM	JJA	OND	DJF	MAM	JJA	OND
CC	10.0	4.0	7.2	4.3	14.2	12.4	6.9	9.9	25.9	11.8	14.4	15.1	8.9	4.6	4.0	3.5
TTS	8.3	4.0	6.3	2.6	14.6	12.4	6.0	7.4	22.2	12.2	13.7	16.0	10.3	5.1	5.0	4.5
NEC	8.1	4.3	5.1	4.0	13.9	9.7	8.1	13.4	12.3	6.8	5.4	7.4	8.8	6.1	2.4	5.0
SEN	3.7	2.9	1.7	2.5	13.5	8.3	6.8	9.6	9.4	7.5	3.0	8.0	5.9	4.0	2.2	3.8
NWP	10.1	8.3	2.6	3.2	8.6	6.9	2.4	3.2	10.7	5.1	7.0	3.2	9.4	7.2	4.3	3.3
PG	5.9	3.2	3.6	2.3	14.7	11.7	5.9	6.2	11.6	9.5	5.1	10.4	6.8	6.0	1.9	2.6
SWC	2.5	1.6	1.2	1.2	7.8	6.7	3.1	2.6	4.4	4.5	0.9	4.1	2.9	3.0	1.4	1.8
SWP	3.6	2.8	1.5	1.3	8.0	7.1	1.8	2.3	5.3	3.9	3.1	2.7	3.1	2.7	0.8	1.4
SAG	2.0	1.6	1.1	1.1	6.6	5.8	2.6	3.6	5.7	5.5	1.1	4.5	4.4	4.2	1.5	1.9
LEB	3.4	1.3	2.7	1.2	10.0	7.9	3.9	6.4	8.9	4.3	4.7	4.9	4.3	2.2	1.4	1.9
MDB	3.3	2.1	2.0	1.6	11.3	7.0	4.2	9.1	6.1	2.8	1.9	4.9	4.7	3.3	1.4	2.8
SEV	3.0	2.3	1.8	1.5	9.5	6.9	2.9	6.3	4.9	4.2	1.5	4.9	4.9	4.5	1.5	2.3
TAS	4.4	3.6	2.7	3.0	6.5	6.7	2.7	3.1	4.5	4.9	2.3	16.0	5.2	4.7	1.7	2.3

Table 7: Long-term linear trend in rainfall variability over various rivers basins across Australia for the period 1981-2014. Please note that the linear trends that are estimated using TMPA products are valid over the period 1998-2014. This, the results from TMPA cannot be directly comparable to those estimated from BoM or other products.

Basin	CC	TTS	NEC	SEN	NWP	PG	SWC	SWP	SAG	LEB	MDB	SEV	TAS
	Overall Trend in Rainfall [mm/decade]												
BoM [1981-2014]	7.3	10.1	2.6	0.0	2.7	1.0	0.0	1.9	0.0	2.4	0.0	0.0	0.0
TMPA [1998-2014]	4.1	0.0	4.4	1.0	-7.1	-3.4	-2.2	-3.8	0.3	4.2	2.7	0.0	-1.0
CHIRP [1981-2014]	3.4	5.0	1.1	0.0	0.0	0.0	0.0	0.0	0.0	0.0	0.0	0.0	0.0
ERA [1981-2014]	-4.2	-13.1	0.0	0.0	-2.8	-0.7	0.0	0.0	0.0	-2.4	-1.4	0.0	0.0
MERRA [1981-2014]	8.8	16.2	2.3	0.0	6.1	1.4	0.0	2.0	0.0	3.1	-1.7	0.0	0.0
	Trends due to ENSO/IOD [mm/decade]												
BoM [1981-2014]	5.9	9.3	2.2	0.0	2.0	1.2	0.0	1.4	0.0	3.0	1.0	0.0	0.0
TMPA [1998-2014]	0.0	-9.9	2.7	0.0	-7.7	-3.5	-1.3	-5.6	0.0	2.1	4.6	0.0	0.0
CHIRP [1981-2014]	2.6	3.5	1.0	0.0	0.4	0.0	0.0	0.0	0.0	0.0	0.0	0.0	0.0
ERA [1981-2014]	-6.1	-14.6	0.0	0.0	-3.9	0.0	0.0	-1.5	0.0	-3.9	0.0	0.0	0.0
MERRA [1981-2014]	7.8	15.3	1.8	0.0	5.6	1.5	0.0	1.6	0.0	3.2	0.0	0.0	0.0

of 2012) that impacted the northern and eastern basins.

5.5. Skills of the satellite and reanalysis products to represent ENSO/IOD events

In Figures 6 and 7, one could see that the dominant behavior of non-seasonal rainfall variations over Australia were significantly influenced by ENSO and IOD events. In order to assess whether the satellite and reanalysis products are in agreement with BoM products, they were projected onto the spatial patterns of Figure 6. This projection allows a consistent comparison by relying on the spatial distribution of rainfall from BoM products, while depicting the temporal patterns with respect to the explained variances of the reference data. Since the grid values located over the northwest and central Australia are almost zero, the performed projection does not include the semi-arid and arid regions, where BoM data is very sparse. The annual and semi-annual cycles were removed and a 5-month running average was applied to each product prior their projections to focus on the impacts of ENSO/IOD on the precipitation residuals. Figure 13 shows the corresponding temporal evolutions of rainfall variability over Australia, which accounted for the total variance of over 35% in non-seasonal rainfall variations. The resulting two evolutions (shown by PCs) in Figures 13a and 13c represented the overal agreement of various products in representing ENSO and IOD impacts.

Figures 13b and 13d show the differences between the evolution of BoM and those derived from projections. In theory, the differences should be zero, while the spatial (shown in the Appendix) and temporal sampling (monthly aggregations) of the assessed products are quite similar. Considering the temporal behavior of residuals, one can see that the temporal patterns of residuals ('biases') are different for the satellite and reanalysis products. ERA-Interim estimates indicated largest difference among the different precipitation estimates over the entire period of 1981 to 2014 with anomalously large overestimation (up to 3 standard deviations) between 1982 and 2000 and large underestimates (up to 3 standard deviations) for the period 2000-2014 (see Figures 13b). Similar results were found for the second mode i.e. Figure 13d. This behavior might be related to the inter-annual biases caused by more pronounced ENSO/IOD activity over the last decade or the existing shifts (over time) in the precipitation differences between ERA-Interim and gauge observations as reported in Simmons et al. (2010). More research should be done to address this issue. On the other hand, the satellite-based CHIRP and reanalysis-based MERRA agreed very well with BoM estimates. The differences were found to be mostly below 1 standard deviation. The TMPA estimates, although with a shorter time period (1998-2014), agreed very well but indicated a periodic underestimation in both modes. This behavior in TMPA can partly originate from the fact that the spatial base function of Figure 6 is not totally fitted to TMPA estimates due to its shorter data coverage. CHIRP and MERRA differences were quite large in the second mode, especially during the active periods of ENSO and IOD phenomena such as in 1998 and 2011 (see, also Figure 7) indicating that rainfall due to major ENSO and IOD events were either underestimated or overestimated. Considering satellite-only estimates (including both infrared and microwave algorithms) over the tropics, Ebert and Manton (1998) found that the advantage of superior temporal and spatial sampling in the geostationary algorithm outweighs the advantage of more directly related measurements of micro-wave estimates in monthly rainfall estimates. This holds true especially over Australia for the IR-based CHIRP products, which indicated relatively low RMSE values and very good skills in describing the inter-annual variability of rainfall over 1981-2014.

Since the biases were amplified during the major ENSO/IOD events, further LSSA analysis was carried out to assess the spectral properties of the large-scale differences between the satellite/reanalysis products and BoM estimates. Figure 14 shows the power spectral density of the first two residual temporal evolutions (as shown in Figures 13b and 13d) of CHIRP (Figure 14a and b) and MERRA (Figure 14c and d). The power spectrum of -Niño 3.4 and -DMI time series are also plotted together to show the structure of ENSO an IOD events in the frequency domain.

The largest peaks in the power spectrum in both products coincided with the peaks in the ENSO and IOD spectrum. For instance, a large peak in PC1 (the first temporal evolution) of CHIRP coincided with the IOD peak (0.28 cycle/year, Figure 14a), while another peak in PC2 (the second temporal evolution) was found close to the largest ENSO peak (0.18 cycle/year, Figure 14b). Peaks in both ENSO and IOD signals were found to coincide with the spectrum of the first temporal evolution of MERRA (0.18 and 0.28 cycle/year, Figure 14c). The spectrum of the second temporal evolution (PC2) in MERRA indicated less correspondence with ENSO and IOD (0.58 cycle/year, Figure 14d). These results further suggest that extreme events such as those related to pronounced ENSO/IOD events represent a significant influence on the difference (or bias) in the satellite and reanalysis rainfall estimates.

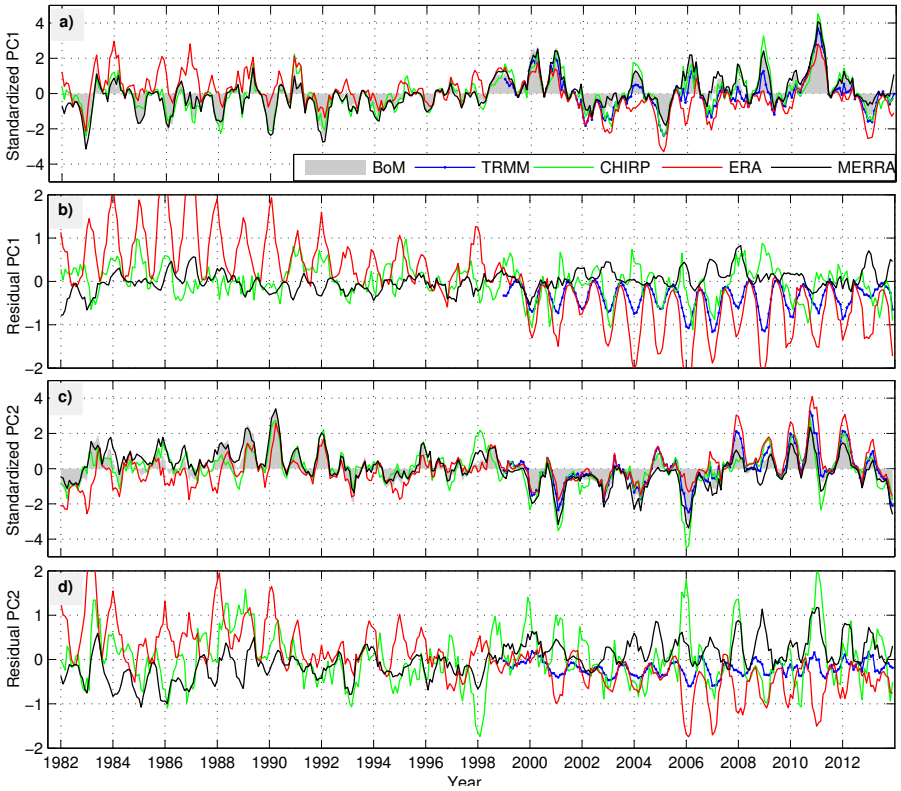

Figure 13: Temporal variability of precipitation error estimates in satellite and reanalysis products. In a and c, the real part of PC1 and PC2 from BoM products are shown along with the temporal evolutions that were estimated by projecting non-seasonal satellite and reanalysis products onto the EOFs of BoM rainfall (Figure 6). In b and d, the residual between the real part of PCs (estimated from BoM products) and the temporal evolutions are shown.

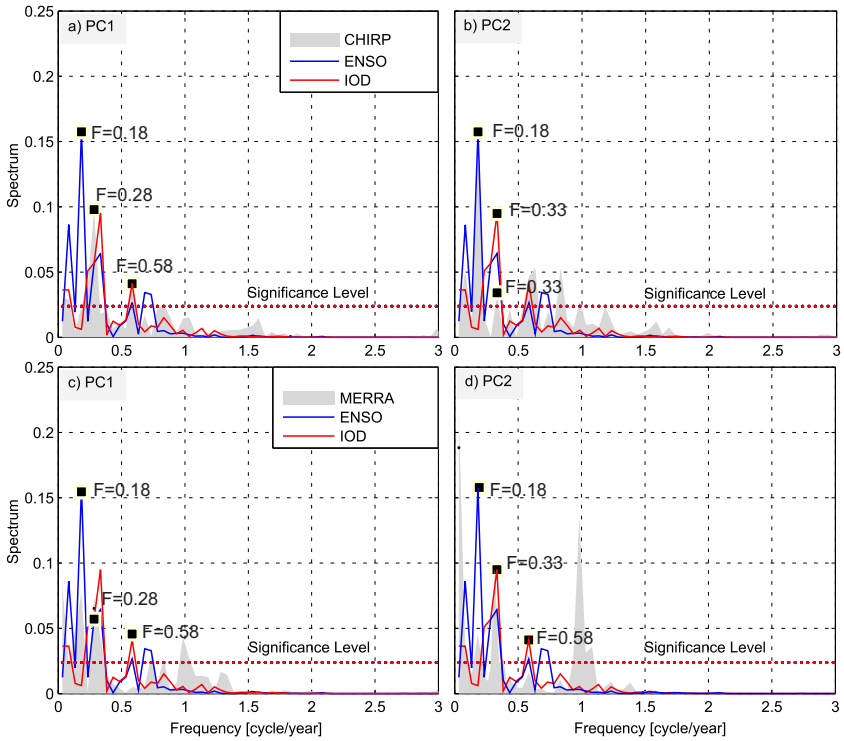

Figure 14: Power spectrum of the first two dominant residuals estimated as the differences between the real part of BoM-PCs (Figure 13) and the temporal evolutions (PCs) of CHIRP (a and b) and MERRA (c and d). Graphs also contain the power spectrum computed while considering the temporal patterns of -Niño 3.4 and -DMI representing the power spectrum density of ENSO and IOD events, respectively.

6. Summary and conclusions

In this study, we investigated the rainfall variability over Australia, including long-term and decadal changes over the period 1981-2014 using various observational and reanalysis gridded precipitation products. The rainfall amounts due to ENSO and IOD were quantified using multi-linear regression (MLR) as well as complex empirical orthogonal functions (CEOF). Two satellite-based (CHIRP and TMPA) and two reanalysis-based (ERA-Interim and MERRA) precipitation products were also evaluated with reference to BoM rainfall products. The decadal and long-term rainfall changes over 1981-2014 were found mainly to be influenced by the combined effect of ENSO and IOD phenomenon by varying degrees. Consistent with previous studies (e.g., Ashok et al., 2003b; Risbey et al., 2009; Ummenhofer et al., 2009a), large regional variations were found for major ENSO/IOD events, which mainly affected the northern and eastern river basins. Rainfall anomalies due to the ENSO and IOD events were found to be often under- or overestimated in global satellite and reanalysis precipitation products. The main results of this study are summarized as follows:

a. A considerable inter-decadal variation were found in Australian rainfall over 1981-2014 in response to 14 weak-strong ENSO events and 12 IOD events contributing up to ∼12% and ∼7% of the total rainfall. The contribution of ENSO/IOD events was more prominent in the past decade due to three consecutive La Niña events (2007-2008, 2008-2009, 2010-2012) despite increasing positive IOD events.
b. After removing the annual and semi-annual signals (using MLR), and applying CEOF to the non-seasonal part, the first two dominant modes were found to represent the impact of ENSO/IOD events. The ENSO/IOD mode of the rainfall, therefore, accounted for 43% of non-seasonal rainfall variability over Australia. The first principal component (temporal pattern) was more correlated to -Niño 3.4 (0.4 at 1 month lag), while -DMI indicated modest correlation with both the PCs (0.24 and 0.34 at 1 month lag). The largest ENSO/IOD impacts were found in the tropical north and the northeast, consistent with the MLR-derived amplitudes (see, Figure 7).
c. Regions of high correlation between ENSO (-Niño 3.4)/IOD (-DMI) and Australian rainfall included tropical Northern Australia, far-west (Western Australia), and eastern Australia with varying degree of magnitudes (see, Figure 10).
d. Long-term and decadal rainfall analyses indicated that increasing rainfall trends over 1981-2014 were largely due to consecutive La Niña events. Specifically during the last 10 years, significant linear trends were found over the majority of the river basins across the northern, northwestern, and eastern Australia. However, no significant increasing or decreasing trends were detected over the Southwest coast and Tasmania.
e. Two satellite-based and two reanalysis-based precipitation products were also used in this study to understand the source of precipitation biases compared to the BoM gauge-based estimates. The results suggested that satellite-based CHIRP and reanalysis-based MERRA products were in good agreement with BoM estimates at inter-annual scale, while ERA-Interim represented considerable positive (1981-2000) and negative (2000-2014) differences with respect to BoM estimates. Overall, the largest deviations occurred in austral summer (December-February), which is the wet season for most of the continent.
f. The differences between the investigated satellite/reanalysis rainfall and BoM products were found to be influenced by extreme climatic conditions resulting from major ENSO/IOD events especially during the La Niña events, where the satellite and reanalysis rainfall estimates were found to be usually underestimated. Thus, an application of a frequency-based bias correction may be useful to reduce the identified biases.

Acknowledgment

The authors are grateful for the comments provided by Prof. Chuanmin Hu (Editor-in-Chief), Prof. Peter Minnett (Associate Editor), and the two anonymous reviewers, which considerably improved the quality of this study. E. Forootan is grateful for the research grant from the German Aerospace Center (DLR, D-SAT project Fkz.: 50 LZ 1402) and the research grant provided by WASM/TIGeR, Curtin University (Australia). Khandu is grateful to Curtin Strategic International Research Scholarship, Curtin

University (Australia), and the Intergovernmental Panel on Climate Change (IPCC) for their valuable scholarships. J. Awange appreciates the financial support from both Alexander von Humboldt and Japan Society of Promotion of Science for his stay at Karlsruhe Institute of Technology (Germany) and Kyoto University (Japan), respectively. M. Schumacher is grateful for the exchange grant (2015/16 57044996) awarded by the German Academic Exchange Service (DAAD) to visit the Australian National University (ANU). The authors are further grateful to the providers of various precipitation products (BoM, TRMM, CHIRP, ERA-Interim, and MERRA), and climate indices used in the study.

References

Ashcroft,L., Karoly, D.J., Gergis, J. (2013), Southeastern Australian climate variability 1860-2009: a multivariate analysis. Int. J. Climatol. published online, doi: 10.1002/joc.3812

Ashok, K., Guan, Z.Y., Yamagata, T. (2003), Influence of the Indian Ocean Dipole on the Australian winter rainfall. Geophys. Res. Lett., 30, 1821, doi:10.1029/2003GL017926

Ashok, K., Z. Guan, and T. Yamagata (2003), A Look at the Relationship between the ENSO and the Indian Ocean Dipole. Journal of the Meteorological Society of Japan, 81, 41-41-56.

Awange, J.L., Anyah, R., Agola, N., Forootan, E., Omondi, P. (2013), Potential impacts of climate and environmental change on the stored water of Lake Victoria Basin and economic implications, Water Resour. Res., 49, 8160-8173, doi:10.1002/2013WR014350

Awange, J., Fleming, K.M., Kuhn, M., Featherstone, W.E., Heck, B., Anjasmara, I. (2011), On the suitability of the $4^\circ \times 4^\circ$ GRACE mascon solutions for remote sensing Australian hydrology. Remote Sensing of Environment, 115 (3), 864-875 http://dx.doi.org/10.1016/j.rse.2010.11.014

Bacchi, B., Kottegoda, N.T. (1995), Identification and calibration of spatial correlation patterns of rainfall, Journal of Hydrology, 165, 311-348,, http://dx.doi.org/10.1016/0022-1694(94)02590-8

Bauer-Marschallinger, B., Dorigo, W.A., Wagner, W., van Dijk, A.I.J.M. (2013), How oceanic oscillation drives soil moisture variations over Mainland Australia: an analysis of 32 years of satellite observations. J. Climate, 26, 10159-10173, doi: http://dx.doi.org/10.1175/JCLI-D-13-00149.1

Best, D.J., Roberts, D.E. (1975), Algorithm AS 89: the upper tail probabilities of Spearman's rho. Applied Statistics, 24:377-379

Bloszies, C., Forman, S. L. (2015), Potential relation between equatorial sea surface temperatures and historic water level variability for Lake Turkana, Kenya, Journal of Hydrology, 520, 489-501, http://dx.doi.org/10.1016/j.jhydrol.2014.10.001

Boening, C., Willis, J.K., Landerer, F.W., Nerem, R.S., Fasullo J. (2012), The 2011 La Niña: So strong, the oceans fell, Geophys. Res. Lett., 39, L19602, doi:10.1029/2012GL053055

Bosilovich, M.G., Chen, J.Y., Robertson, F.R., Adler, R.F. (2008), Evaluation of global precipitation in reanalyses. J. Appl. Meteor. Climatol., 47, 2279-2299, doi: http://dx.doi.org/10.1175/2008JAMC1921.1

Bromwich, D.H., Nicolas, J.P., Monaghan, A.J. (2011), An assessment of precipitation changes over Antarctica and the Southern Ocean since 1989 in contemporary global reanalyses. J. Climate, 24, doi: 10.1175/2011JCLI4074.1

Brook, R.J., Arnold, G.C. (1985), Applied regression analysis and experimental design. CRC Press, New York, 256pp, ISBN:978-0824772529

Cai, W., van Rensch, P., Cowan, T., Hendon, H.H. (2011), Teleconnection Pathways of ENSO and the IOD and the Mechanisms for Impacts on Australian Rainfall. J. Climate, 24, 3910-3923, doi: http://dx.doi.org/10.1175/2011JCLI4129.1

650 Cai, W., van Rensch, P., Cowan, T., Hendon, H.H. (2012), An Asymmetry in the IOD and ENSO
651 Teleconnection Pathway and Its Impact on Australian Climate. J. Climate, 25, 6318-6329. doi:
652 http://dx.doi.org/10.1175/JCLI-D-11-00501.1

653 Cai, W. and van Rensch, P. (2012), The 2011 southeast Queensland extreme summer rainfall: A con-
654 firmation of a negative Pacific Decadal Oscillation phase? Geophysical Research Letters, 39(8). doi:
655 0.1029/2011GL050820

656 Chen, Y., Ebert, E.E., Walsh, K.J.E., Davidson, N.E. (2013), Evaluation of TRMM 3B42 precipi-
657 tation estimates of tropical cyclone rainfall using PACRAIN data, J. Geophys. Res. Atmos., 118,
658 doi:10.1002/jgrd.50250

659 Chiew, F., Piechota, T., Dracup, J., McMahon, T. (1998), El Niño/Southern Oscillation and Aus-
660 tralian rainfall, streamflow and drought: Links and potential for forecasting. J. Hydrol., 204, 138-149,
661 doi:10.1016/S0022-1694(97)00121-2

662 Córdoba-Machado, S., Palomino-Lemus, R., Gámiz-Fortis, S.R., Castro-Díez, Y., Esteban-Parra, M.J.
663 (2015), Assessing the impact of El Niño Modoki on seasonal precipitation in Colombia, Global and
664 Planetary Change, 124, 1-61, http://dx.doi.org/10.1016/j.gloplacha.2014.11.003

665 de Linage, C., Kim, H., Famiglietti, J.S., Yu, J.-Y. (2013), Impact of Pacific and Atlantic sea surface
666 temperatures on interannual and decadal variations of GRACE land water storage in tropical South
667 America, J. Geophys. Res. Atmos., 118, 10,811-10,829, doi:10.1002/jgrd.50820

668 Dai, A. (2013), Increasing drought under global warming in observations and models. Nat. Climate
669 Change, 3, 52-58, doi:10.1038/nclimate1633

670 Dee, D.P., and Coauthors, (2011), The ERA-Interim reanalysis: configuration and performance of the
671 data assimilation system. Quart. J. Roy. Meteor. Soc., 137, 553-597

672 Donat, M.G., Sillmann, J., Wild, S., Alexander, L.V., Lippmann, T., Zwiers, F.W. (2014), Consistency
673 of temperature and precipitation extremes across various global gridded in situ and reanalysis datasets.
674 J. Climate, 27, 5019-5035. doi: http://dx.doi.org/10.1175/JCLI-D-13-00405.1

675 Drosdowsky, W. (1993), An analysis of Australian seasonal rainfall anomalies: 19501987. II: Temporal
676 variability and teleconnection patterns. Int. J. Climatol., 13: 111149. doi: 10.1002/joc.3370130202

677 Ebert, E.E., Janowiak, J.E., Kidd, C. (2007), Comparison of near-realtime precipitation estimates from
678 satellite observations and numerical models. Bull. Amer. Meteor. Soc., 88, 1-47

679 Ebert, E.E., Manton M.J. (1998), Performance of Satellite Rainfall Estimation Algorithms during
680 TOGA COARE. J. Atmos. Sci., 55, 1537–1557. doi: http://dx.doi.org/10.1175/1520-0469(1998)
681 055<1537:POSREA>2.0.CO;2

682 Enfield, D.B., Mestas-Nuñez, A.M. (1999), Multiscale Variabilities in Global Sea Surface Tempera-
683 tures and Their Relationships with Tropospheric Climate Patterns. J. Climate, 12, 2719-2733, doi:
684 http://dx.doi.org/10.1175/1520-0442(1999)012¡2719:MVIGSS¿2.0.CO;2

685 Fitzpatrick, E. A. (1964), Seasonal distribution of rainfall in Australia analysed by Fourier methods.
686 Archiv für Meteorologie, Geophysik und Bioklimatologie, 13(2), 270-286, doi: 10.1007/BF02243257

687 Fleming, K., Awange, J. (2013). Comparing the version 7 TRMM 3B43 monthly precipitation product
688 with the TRMM 3B43, version 6/6A and Bureau of Meteorology datasets for Australia. Australian
689 Meteorological and Oceanographic Journal, 63, 3, p. 421-426.

690 Forootan, E., Awange, J., Kusche, J., Heck, B., Eicker, A. (2012), Independent patterns of water
691 mass anomalies over Australia from satellite data and models. Remote Sens. Environ., 124, 427-443,
692 doi:10.1016/j.rse.2012.05.023

693 Forootan, E. (2014), Statistical signal decomposition techniques for analyzing time-variable
694 satellite gravimetry data. PhD thesis, University of Bonn, pp131, http://hss.ulb.uni-
695 bonn.de/2014/3766/3766.htm

696 Fu, G., Viney, N.R., Charles, S.P., Liu, J. (2010). Long-term temporal variation of extreme rainfall events
697 in Australia: 1910-2006. J. Hydrometeor, 11, 950-965. doi: http://dx.doi.org/10.1175/2010JHM1204.1

698 Funk, C., Michaelsen, J., Marshall, M.T. (2012), Mapping recent decadal climate variations in precipita-
699 tion and temperature across eastern Africa and the Sahel, in Remote Sensing of Drought: Innovative
700 Monitoring Approaches, edited by B. D. Wardlow, M. C. Anderson, and J. P. Verdin, Chap. 14, pp.
701 331-357, CRC Press 2012

702 Funk, C.C., Peterson, P.J., Landsfeld, M.F., Pedreros, D.H., Verdin, J.P., Rowland, J.D., Romero, B.E.,
703 Husak, G.J., Michaelsen, J.C., Verdin, A.P. (2014), A quasi-global precipitation time series for drought
704 monitoring, U.S. Geological Survey Data Series, 27, 1062-1069, doi: 10.1175/JCLI-D-13-00332.1

705 Gebremichael, M., Zeweldi, D.A. (2007), Evaluating satellite rainfall products and their impacts in
706 hydrologic model simulations, Eos Trans. AGU, 88(52), Fall Meet. Suppl., Abstract, San Francisco,
707 CA, USA, December 2007

708 Garćia-Garćia, D., Ummenhofer, C.C., Zlotnicki, V. (2011). Australian water mass variations from
709 GRACE data linked to Indo-Pacific climate variability. Remote Sens. Environ., 115, 2175-2183,
710 doi:10.1016/j.rse.2011.04.007.

711 Hendon, H. H., D. W. J. Thompson, and M. C. Wheeler (2007), Australian Rainfall and Surface Temper-
712 ature Variations Associated with the Southern Hemisphere Annular Mode. J. Climate, 20, 2452-2467,
713 doi: http://dx.doi.org/10.1175/JCLI4134.1

714 Horel, J.D. (1984), Complex principal component analysis: theory and examples. J. Climate Appl.
715 Meteor., 23, 1660-1673, doi: http://dx.doi.org/10.1175/1520-0450(1984)023¡1660:CPCATA¿2.0.CO;2

716 Huffman, G., Adler, R., Bolvin, D., Gu, G., Nelkin, E., Bowman, K., Hong, Y., Stocker, E.,
717 Wolff, D. (2007). The TRMM multisatellite precipitation analysis (TMPA): Quasi-global, multi-
718 year, combined-sensor precipitation estimates at fine scales. Journal of Hydrometeorology, 8(1), 38-55,
719 doi:10.1175/JHM560.1

720 Huffman, G.J., Bolvin, D.T. (2013), TRMM and other data precipitation data set documentation, Tech.
721 rep., Mesoscale Atmospheric Processes Laboratory, NASA Goddard Space Flight Center and Science
722 Systems and Applications, Inc.

723 Jones, D., Wang, W., Fawcett, R. (2009), High-quality spatial climate data-sets for Australia. Australian
724 Meteorological and Oceanographic Journal, 58(4), 233-248

725 Li, X.-F., Yu, J., Li, Y. (2013), Recent Summer Rainfall Increase and Surface Cooling over Northern
726 Australia since the Late 1970s: A Response to Warming in the Tropical Western Pacific. J. Climate,
727 26, 7221-7239 doi: http://dx.doi.org/10.1175/JCLI-D-12-00786.1

728 Liu, Y., van Dijk, A.I.J.M., de Jeu, R.A.M., Holmes, T.R.H. (2009), An analysis of spatiotemporal
729 variations of soil and vegetation moisture from a 29-year satellite-derived data set over mainland
730 Australia, Water Resour. Res., 45, W07405, doi:10.1029/2008WR007187.

731 Liu, Y., de Jeu, R.A.M., van Dijk, A. I.J.M., Owe, M. (2007), TRMM-TMI satellite observed soil
732 moisture and vegetation density (1998-2005) show strong connection with El Niño in eastern Australia,
733 Geophys. Res. Lett., 34, L15401, doi:10.1029/2007GL030311.

734 Los, S. O (2014), Testing gridded land precipitation data and precipitation and runoff reanalyses (1982-
735 2010) between 45° S and 45° N with normalized difference vegetation index data. Hydrol. Earth Syst.
736 Sci. Discuss., 11, 13175-13205, doi:10.5194/hessd-11-13175-2014

737 Newman, M., G. P. Compo and M. A. Alexander (2003), ENSO-Forced Variability of the Pacific
738 Decadal Oscillation. J. Climate, 16, 3853-3857, doi: http://dx.doi.org/10.1175/1520-0442(2003)
739 016<3853:EVOTPD>2.0.CO;2

740 Nicholls, N. (1985), Towards the prediction of major Australian droughts. Aust. Meteor. Mag., 33,
741 161-166.

742 Nicholls, N., Drosdowsky, W., Lavery, B. (1997), Australian rainfall variability and change. Weather 52:
743 66-72

744 Nicholls, N (2006), Detecting and attributing Australian climate change: a review. Aust. Met. Mag., 55,
745 199-211, doi:10.1.1.222.8103

746 Nicholls, N (2010), Local and remote causes of the southern Australian autumn-winter rainfall decline,
747 1958-2007. Climate Dynamics, 34(6), 835–845, doi: 10.1007/s00382-009-0527-6.

748 Omondi, P., Awange, J.L., Ogallo, L.A.,Ininda, J., Forootan, E. (2013), The influence of low frequency
749 sea surface temperature modes on delineated decadal rainfall zones in Eastern Africa region, Advances
750 in Water Resources, 54, 161-180, http://dx.doi.org/10.1016/j.advwatres.2013.01.001

751 Peña-Arancibia, J.L., van Dijk, A.I.J.M., Renzullo, L.J., Mulligan, M. (2013), Evaluation of precipitation
752 estimation accuracy in reanalyses, satellite products, and an ensemble method for regions in Australia
753 and South and East Asia. J. Hydrometeor, 14, 1323-1333. doi: http://dx.doi.org/10.1175/JHM-D-12-
754 0132.1

755 Peña-Arancibia, J.L., van Dijk, A.I.J.M., Stenson, M.P., Viney, N.R. (2011), Opportunities to evaluate
756 a landscape hydrological model (AWRA-L) using global data sets. 19th International Congress on
757 Modelling and Simulation, Perth, Australia, 12-16 December 2011

758 Phillips, T., Nerem, R.S., Fox-Kemper, B., Famiglietti, J.S., Rajagopalan, B. (2012), The influ-
759 ence of ENSO on global terrestrial water storage using GRACE, Geophys. Res. Lett., 39, L16705,
760 doi:10.1029/2012GL052495

761 Pipunic, R.C., Ryu, D., Costelloe, J., Su, C-H. (2013), Evaluation of real-time satellite rainfall prod-
762 ucts in semi-arid/arid Australia. 20th International Congress on Modelling and Simulation, Adelaide,
763 Australia, 1-6 December 2013

764 Pook, M.J., Risbey, J.S., McIntosh, P.C., Ummenhofer, C.C., Marshall, A.G., Meyers, G.A. (2013), The
765 seasonal cycle of blocking and associated physical mechanisms in the Australian region and relationship
766 with rainfall. Mon. Wea. Rev., 141, 4534-4553, doi: http://dx.doi.org/10.1175/MWR-D-13-00040.
767 1

768 Power, S., Casey, T., Folland, C., Colman, A., Mehta, V. (1999), Inter-decadal modulation of the impact
769 of ENSO on Australia. Climate Dynamics, 15, 319-324, doi:10.1007/s003820050284

770 Preisendorfer, R. (1988), Principal component analysis in meteorology and oceanography. Elsevier: Am-
771 sterdam, 444pp, ISBN: 978-0444430144

772 Rasmusson, E.M., Arkin, P.A., Chen, W-Y., Jalickee, J.B. (1981), Biennial variations in surface tem-
773 perature over the United States as revealed by singular decomposition. Monthly Weather Review,
774 109:587-598

775 Raut, B.A., Jakob, C., Reeder, M.J. (2014), Rainfall changes over southwestern Australia and
776 their relationship to the Southern Annular Mode and ENSO. J. Climate, 27, 5801-5814, doi:
777 http://dx.doi.org/10.1175/JCLI-D-13-00773.1

778 Renzullo, L.J., Chappell, A., Raupach, T., Dyce, P., Ming, L., Shao, Q. (2011), An assessment of
779 statistically blended satellite-gauge precipitation data for daily rainfall analysis in Australia. 34th
780 International Symposium on Remote Sensing of Environment, Sydney 11-15 April 2011

Rienecker, M.M., and Coauthors, (2011), MERRA: NASA's Modern-Era retrospective analysis for research and applications. J. Climate, 24, 3624-3648

Risbey, J. S., M. J. Pook, P. C. McIntosh, M. C. Wheeler, H. H. Hendon, (2009), On the remote drivers of rainfall variability in Australia. Mon. Wea. Rev., 137, 3233-3253. doi: http://dx.doi.org/10.1175/2009MWR2861.1

Rieser, D., Kuhn, M., Pail, R., Anjasmara, I.M., Awange, J. (2011), Relation between GRACE-derived surface mass variations and precipitation over Australia. Australian Journal of Earth Sciences, 57 (7), 887-900, http://dx.doi.org/10.1080/08120099.2010.512645

Saji, N.H., Goswami, B. N., Vinayachandran, P. N., Yamagata, T. (1999), A dipole mode in the tropical Indian Ocean. Nature, 401, 360-363.

Saji N.H., Yamagata, T. (2003), Structure of SST and surface wind variablity during Indian Ocean Dipole Mode events: COADS observations. American Meteorological Society, 16, 2735-2751

Schneider, U., Becker, A., Finger, P., Meyer-Christopher, A., Ziese, M., Rudolf, B. (2014), GPCC's new land surface precipitation climatology based on quality-controlled in situ data and its role in quantifying the global water cycle. Theoretical and Applied Climatology, 115 (1-2), 15-40, doi:10.1007/s00704-013-0860-x

Seoane,L., Ramillien, G., Frappart, F., Leblanc, M. (2013), Regional GRACE-based estimates of water mass variations over Australia: validation and interpretation. Hydrol. Earth Syst. Sci., 17, 4925-4939, doi:10.5194/hess-17-4925-2013

Sharifi, M.A. , Forootan, E., Nikkhoo, M., Awange, J.L., Najafi-Alamdari M. (2013), A point-wise least squares spectral analysis (LSSA) of the Caspian Sea level fluctuations, using TOPEX/Poseidon and Jason-1 observations. Advances in Space Research, 51 (5), 858-873, http://dx.doi.org/10.1016/j.asr.2012.10.001

Simmons, A.J., Willett, K.M., Jones, P.D., Thorne, P.W., Dee, D.P. (2010), Low-frequency variations in surface atmospheric humidity, temperature, and precipitation: Inferences from reanalyses and monthly gridded observational data sets. J. Geophys. Res., 115, D01110, doi:10.1029/2009JD012442

Smith I.N. (2004), An assessment of recent trends in Australian rainfall. Australian Meteorological Magazine. 53: 163-173

Smith, I.N., Collier, M., Rotstayn, L. (2009), Patterns of summer rainfall variability across tropical Australia - results from EOT analysis. 18'th World IMACS / MODSIM Congress, Cairns, Australia 13-17 July 2009

Stern, H., de Hoedt, G., Ernst, J. (2000), Objective classification of Australian climates. Australian Meteorological Magazine, 49(2), 87-96

Sturman, A.P., Tapper N.J. (1996), Weather and climate of Australia and New Zealand. Oxford University Press, Melbourne, 476 pp

Taschetto, A.S., England, M. H. (2009), An analysis of late twentieth century trends in Australian rainfall. International Journal of Climatology, 29(6), 791-807, doi: 10.1002/joc.173

Trenberth, K.E. (1990), Recent observed interdecadal climate changes in the Northern Hemisphere. Bulletin of the American Meteorological Society 71: 988-993, doi: http://dx.doi.org/10.1175/1520-0477(1990)071¡0988:ROICCI¿2.0.CO;2

Trenberth, K.E. (2011). Changes in precipitation with climate change. Climate Res., 47, 123-138, doi:10.3354/cr00953

Ummenhofer, C.C., England, M.H., McIntosh, P.C., Meyers, G.A., Pook, M.J., Risbey, J.S., Sen Gupta, A., Taschetto, A.S. (2009), What causes southeast Australia's worst droughts? Geophys. Res. Lett., 36, L04706, doi:10.1029/2008GL036801

Ummenhofer, C.C., Sen Gupta, A., Taschetto, A.S., England, M.H. (2009b), Modulation of Australian precipitation by meridional gradients in East Indian Ocean sea surface temperature. J. Clim., 22, 5597-5610

van Dijk, A.I.J.M., Beck, H.E., Crosbie, R.S., de Jeu, R.A.M., Liu, Y. Y., Podger, G. M., Timbal, B., Viney, N.R. (2013), The Millennium Drought in southeast Australia (2001-2009): Natural and human causes and implications for water resources, ecosystems, economy, and society. Water Resour. Res., 49, 1040-1057, doi:10.1002/wrcr.20123

van Dijk, A.I.J.M., Renzullo, L.J., Rodell, M. (2011), Use of Gravity Recovery and Climate Experiment terrestrial water storage retrievals to evaluate model estimates by the Australian water resources assessment system, Water Resour. Res., 47, W11524, doi:10.1029/2011WR010714.

Van Dijk, A.I.J.M., Renzullo, L.J. (2011), Water resource monitoring systems and the role of satellite observations. Hydrol. Earth Syst. Sci., 15, 39-55, doi:10.5194/hess-15-39-2011

Vanicék, P. (1969), Approximate spectral analysis by least-squares fit. Successive spectral analysis. Astrophys. Space Sci. 4, 387-391, http://dx.doi.org/ 10.1007/BF00651344.

Walker, G. T. (1923), Correlations in seasonal variations in weather, VIII. Mem. India Meteor. Dept., 24, 75-131.

Weymouth, G., Mills, G.A., Jones, D., Ebert, E.E., Manton, M.J. (1999). A continental-scale daily rainfall analysis system. Aust. Met. Mag., 48, 169-179.

Wheeler, M.C., Hendon, H.H., Cleland, S., Meinke, H., Donald, A. (2009), Impacts of the Madden-Julian Oscillation on Australian Rainfall and Circulation. J. Climate, 22, 1482-1498, doi: http://dx.doi.org/10.1175/2008JCLI2595.1

Appendix A - Spatial representation of the satellite and reanalysis products

To evaluate the spatial variability of various precipitation products over Australia, spatial correlation lengths were calculated from the mean reduced differences of BoM products and each of the satellite and reanalysis precipitation estimates. The differences were computed based on the mean seasonal rainfall of the four seasons December-January-February (DJF), March-April-May (MAM), June-July-August (JJA), and September-October-November (SON). A spatial autocorrelation has been estimated to assess the distance of spatial dependence between each pair of grid point. Figure A1a represents the empirical and analytical correlation functions, which has been determined by fitting a simple exponential function, exemplified by TMPA products considering the four seasons. Results for the other products were found to be quite similar.

Previous studies reported that the spatial correlations of above ~ 0.2 between various precipitation estimates (products) cannot be neglected (e.g., Bacchi and Kottegoda, 1995). Therefore, the correlation value of 0.2 in Figure A1a is chosen to present the spatial correspondence of available satellite/reanalysis products against BoM during the four DJF, MAM, JJA, and SON seasons, see e.g., Figure A1b. The variability between the four seasons was found to be small for CHIRP and ERA-Interim ($\sim 40-50$ km), while that of TMPA and MERRA indicated differences of ~ 150 and ~ 200 km, respectively. The length differences were found between JJA/MAM and DJF/SON seasons showing that during the wet season products were closer to BoM than the dry seasons. A comparable spatial representation was found for CHIRP, ERA-Interim and TMPA with $\sim 200-300$ km correlation length. MERRA was found to be slightly different from the other products exhibiting less spatial correspondence to BoM (with the length of ~ 500 km). By considering another threshold value (a correlation different from 0.2 graphs in Figure A1a), the spatial correlation lengths in Figure A1b will be changed, i.e., selecting bigger threshold would lead to smaller spatial distance. However, the overall behavior of the four lines in Figure A1b would not be changed.

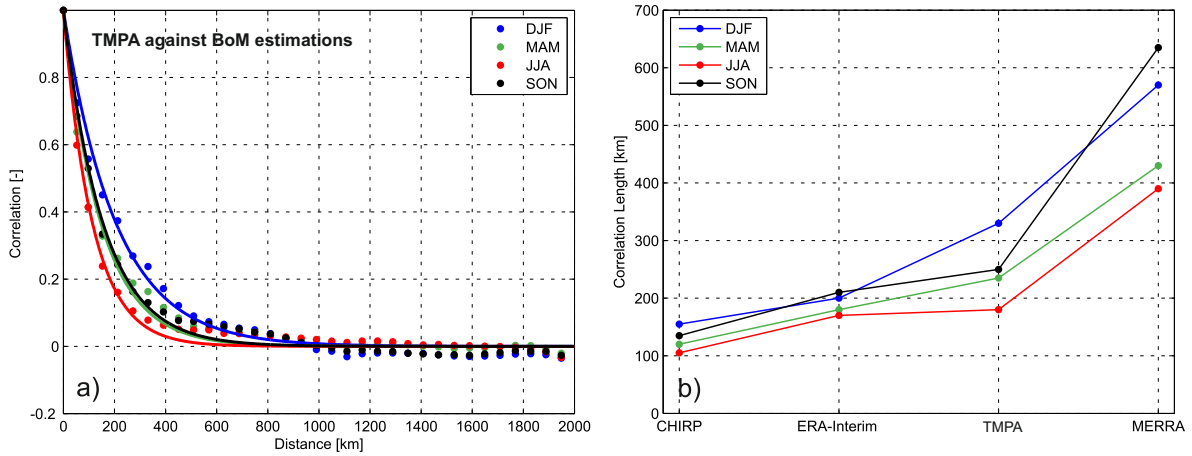

Figure A1a) Empirical (dots) and analytical (lines) spatial correlation functions exemplified by TMPA rainfall product when analyzing the differences to the reference dataset BoM corresponding to four seasons of DJF, MAM, JJA, and SON. Figure A1b) Correlation length in km (defined as the distance according to correlation value 0.2 in Figure A1a) estimated from the seasonal differences of BoM products and the four rainfall products of CHIRP, TMPA, ERA-Interim, and MERRA.